

Statistical detection of clumps and gaps in a random sample by continuous wavelet transforms: the 2D case

Roman V. Baluev^{a,b}, Evgeniy I. Rodionov^b, Vakhit Sh. Shaidulin^b

^aCentral Astronomical Observatory at Pulkovo of Russian Academy of Sciences, Pulkovskoje sh. 65/1, St Petersburg 196140, Russia

^bSaint Petersburg State University, Faculty of Mathematics and Mechanics, Universitetskij pr. 28, Petrodvorets, St Petersburg 198504, Russia

Abstract

We present a self-consistent framework to perform the wavelet analysis of two-dimensional statistical distributions. The analysis targets the 2D probability density function (p.d.f.) of an input sample, in which each object is characterized by two peer parameters. The method performs a probabilistic detection of various ‘patterns’, or ‘structures’ related to the behaviour of the p.d.f. Laplacian. These patterns may include regions of local convexity or local concavity of the p.d.f., in particular peaks (groups of objects) or gaps. In the end, the p.d.f. itself is reconstructed based on the least noisy (most economic) superposition of such patterns. Among other things, our method also involves optimal minimum-noise wavelets and minimum-noise reconstruction of the distribution density function.

The new 2D algorithm is now implemented and released along with an improved and optimized 1D version. The code relies on the C++11 language standard, and is fully parallelized.

The algorithm has a rich range of applications in astronomy: Milky Way stellar population analysis, investigations of the exoplanets diversity, Solar System minor bodies statistics, etc.

Keywords: Astronomy data analysis, Wavelet analysis, Nonparametric inference, Computational methods, Astrostatistics techniques, Main belt asteroids

1. Introduction

The wavelet analysis, ascending in its early form to Grossman and Morlet (1984), is a mathematical tool that allows to decompose a function into multiple levels of different resolutions.

Nowdays, the wavelet analysis technique is frequently used in various fields of astronomy. The single-dimensional version is useful in the time series analysis, because it allows to track the time evolution of quasi-periodic variations (Foster, 1996), while two-dimensional wavelets are often used in the image analysis.

However, most of these classic applications of wavelets target functions of some deterministic ar-

gument x (where x can be from \mathbb{R}^n in general). Although the function itself, $f(x)$, may contain random noise, this function is assumed to be defined on some continuous domain or on a fine enough grid to approximate this continuous domain. In this case we just measure the values $f_i = f(x_i)$ and apply a discretized version of the wavelet transform to these values. But in this work we consider the application of the wavelet technique to a not so popular but still practically important task: analyse a probability density function $f(x)$ of some random variable, or a pair of (possibly correlated) random variables. In this case we do not measure any f_i at all. Instead, we should estimate the wavelet transform based on some finite-size statistical sample $\{x_i\}_{i=1}^N$. Here the function $f(x)$ is determined implicitly, as a local density of these x_i in the vicinity of the specified point x .

Email address: r.baluev@spbu.ru (Roman V. Baluev)

As we can see, the mathematical formulation of this task is qualitatively different from what is used in the classic wavelet analysis.

The single-dimensional case of this task was already considered in (Baluev, 2018), with an application to exoplanetary distributions presented in (Baluev and Shaidulin, 2018). In this work, we present an extension of the 1D theory to the case of two dimensions. The 2D case is even more practical perhaps, since it is considerably more informative than the 1D one: various statistical families can often be resolved from each other in 2D, even if they overlap in the both 1D distributions. Therefore, 2D analysis of statistical samples can be useful in multiple fields: Milky Way population studies, especially in view of the emerging GAIA data (Brown et al., 2018), statistical and dynamical studies of asteroids in Solar System, studies of exoplanetary statistics, which now became quite reach thanks to the ground-based as well as space projects like Kepler and the ongoing TESS.

Unfortunately, there is only a relatively meagre amount of literature available with respect to the analysis of statistical distributions by wavelets. First attempts to apply the wavelet transform technique to reveal clumps in stellar distributions date back to 1990s (Chereul et al., 1998; Skuljan et al., 1999), and Romeo et al. (2003, 2004) suggested the use of wavelets for denoising results of N -body simulations. Nowadays, wavelet transforms are quite routinely used to analyse CMB data from WMAP (McEwen et al., 2004, 2017). The very idea of ‘wavelets for statistics’ from the mathematical point of view was also considered by Fadda et al. (1998); Abramovich et al. (2000).

But after a closer look, many of these wavelet analysis methods appeared deficient in some aspects. This discussion is given in details in (Baluev, 2018), and here we highlight only two main issues. The first one is that the wavelet transform is often applied to a binned sample. This allows to use merely the classic wavelet analysis technique with only minor modifications concerning the noise treatment (the noise in each bin or 2D box appears Poisson rather than Gaussian). However such an approach implies obvious caveats: the binning always leads to (i) losing the small-scale resolution and (ii) additional interpolation-like errors. Yet another issue appears

when thresholding the noise in the wavelet transform. To perform such a thresholding, we obviously must determine some significance level for wavelet coefficients. However, since in practice we always consider a large domain in the shift-scale space rather than just a single point, it is necessary to consider the significance of multiple coefficients at once, rather than each individually. This means that the significance levels must be determined based on the corresponding extreme value distribution (EVD), rather than single value distribution (SVD). This issue has often been ignored in the literature, e.g. by Skuljan et al. (1999), but then our analysis result may occur to depend on a single outlier wavelet coefficient, which become increasingly more frequent if we expand the analysis domain. Another issue with the significance levels appear because they are usually computed from Monte Carlo simulations, which is a very slow and heavy computation. The need of analytic significance formulae therefore becomes obvious.

In this paper we mainly present the mathematical theory from (Baluev, 2018) extended to the 2D case, and describe our new optimized computing code (both for the 1D and 2D cases). Below we also provide a quick 2D test case to demonstrate the practical use of our algorithm and its possible benefits. However, in this paper we did not intend to do a comprehensive ‘field-testing’ of the code or to apply it to a particular sample of objects. The latter task is left for future work.

The code is available for download at <https://sourceforge.net/projects/waveletstat/>. It is open-source and licensed under the MIT license. The download archive also contains an 1D sample test case application (sample data, code invocation script, and GNUPLOT script to render the results in graphical form)

2. Overview of the paper

In this paper we undertook an extensive work following generally the same sequence as in the 1D case (Baluev, 2018).

1. We start from presenting some basic mathematical definitions, general discussion and justification of the method (Sect. 3).

2. Further on, we present a self-consistent statistical theory, including the sample-based estimation of the Continuous Wavelet Transform (or CWT), construction of the statistical tests and analytic calibration of the CWT noise levels and its normality (Sect. 4).
3. Then we find optimal wavelets that provide minimum noise, simultaneously constraining the CWT noise at a high order of normality, as well as an optimal minimum-noise reconstruction kernel for the inverse CWT (Sect. 5).
4. We discuss an iterative matching pursuit like algorithm that builds a p.d.f. model based on CWT noise thresholding (Sect. 6).
5. In Sect. 7, we discuss our updated 1D and new 2D code that efficiently implement all this theory.
6. In Sect. 8 we present some numeric tests to verify the statistical validity of our 2D algorithm, and also a demonstrative example exposing an analysing of a 2D distribution of the Main belt asteroids.

3. Wavelet transforms in two or more dimensions: basic mathematics

3.1. Definitions of the CWT in multiple dimensions

The first definition of the CWT uses the shift (or location) n -dimensional vector \mathbf{b} and the $n \times n$ scale matrix \mathbf{A} . We will call it the Y -shape:

$$Y(\mathbf{A}, \mathbf{b}) = \int f(\mathbf{x})\psi(\mathbf{A}^{-1}(\mathbf{x} - \mathbf{b}))d\mathbf{x}. \quad (1)$$

Alternatively, the so-called Υ -shape might be convenient sometimes:

$$\Upsilon(\mathbf{K}, \mathbf{c}) = \int f(\mathbf{x})\psi(\mathbf{K}\mathbf{x} + \mathbf{c})d\mathbf{x}. \quad (2)$$

It involves the phase-like vector argument \mathbf{c} and the wavenumber-like matrix argument \mathbf{K} .

These Y -shape and Υ -shape formulae define exactly the same quantity, parametrized by different systems of independent variables. These variables are mutually bound as:

$$\mathbf{A} = \mathbf{K}^{-1}, \quad \mathbf{c} = -\mathbf{K}\mathbf{b}. \quad (3)$$

This assumes that \mathbf{K} is always non-degenerate, so that \mathbf{A} exists. All the quantities, vectors and matrices above are assumed real.

We can alternatively rewrite the Y -shape as

$$Y(\mathbf{A}, \mathbf{b}) = |\det \mathbf{A}| \int f(\mathbf{b} + \mathbf{A}\mathbf{t})\psi(\mathbf{t})d\mathbf{t}. \quad (4)$$

If ψ is well-localized, which is true for what we call ‘wavelet’, then such ψ basically cuts in $f(\mathbf{x})$ a domain centered at \mathbf{b} and sized and shaped according to the scale parameters from the matrix \mathbf{A} .

This very general definition of the CWT implies $n + n^2 = n(n + 1)$ degrees of freedom. Already in the 2D case, $n = 2$, this results in 6 degrees of freedom, which is probably too large to be practical.

Now let us assume that our wavelet is radially symmetric:

$$\psi(\mathbf{t}) = \psi(t). \quad (5)$$

Then let us write

$$t^2 = (\mathbf{x} - \mathbf{b})^T(\mathbf{K}^T\mathbf{K})(\mathbf{x} - \mathbf{b}). \quad (6)$$

As we can see, in this case the CWT depends on the real symmetric positive-definite matrix $\mathbf{K}^T\mathbf{K}$, implying the reduction of total number of degrees of freedom from $n(n + 1)$ to $n + n(n + 1)/2 = n(n + 3)/2$.

Since $\mathbf{K}^T\mathbf{K}$ is real symmetric positive-definite matrix, let us diagonalize it:

$$\mathbf{K}^T\mathbf{K} = \mathbf{R}^T\mathbf{D}\mathbf{R}, \quad \mathbf{D} = \text{diag}(\kappa_i^2), \quad \kappa_i = 1/a_i. \quad (7)$$

Here, \mathbf{R} is an orthogonal matrix. Such an \mathbf{R} may describe, in general, any isometry transform in \mathbb{R}^n that includes e.g. rotations, reflections, and permutations. However, reflections and permutations do not provide any useful new information, so we restrict \mathbf{R} to be a rotation matrix.

Then, without loss of generality, we may set

$$\mathbf{K} = \mathbf{D}^{1/2}\mathbf{R}, \quad \mathbf{A} = \mathbf{R}^T\mathbf{D}^{-1/2}, \quad \mathbf{c} = -\mathbf{D}^{1/2}\mathbf{R}\mathbf{b}. \quad (8)$$

This implies,

$$\begin{aligned} Y(\mathbf{a}, \mathbf{R}, \mathbf{b}) &= \int f(\mathbf{x})\psi\left(\left|\frac{\mathbf{R}(\mathbf{x} - \mathbf{b})}{\mathbf{a}}\right|\right)d\mathbf{x} \\ &= |a_1 \dots a_n| \int f(\mathbf{b} + \mathbf{R}^T(\mathbf{a} \odot \mathbf{t}))\psi(\mathbf{t})d\mathbf{t}, \end{aligned} \quad (9)$$

where \odot stands for the coordinatewise vector multiply operation, and the division of vector arguments $\frac{*}{*}$ is also understood coordinatewisely.

Finally, we introduce the so-called entirely isotropic case. Now we restrict the scale matrix \mathbf{A} so that it is reduced to just a single scalar parameter: $\mathbf{D} = \kappa^2 \mathbf{I}$, $\kappa = 1/a$, and $\mathbf{R} = \mathbf{I}$. This yields

$$Y(a, \mathbf{b}) = \int f(\mathbf{x}) \psi \left(\frac{|\mathbf{x} - \mathbf{b}|}{a} \right) d\mathbf{x},$$

$$\Upsilon(\kappa, \mathbf{c}) = \int f(\mathbf{x}) \psi (|\kappa \mathbf{x} + \mathbf{c}|) d\mathbf{x}, \quad \mathbf{c} = -\kappa \mathbf{b}. \quad (10)$$

This case involves just $n + 1$ degrees of freedom.

We add a note that $Y(a, \mathbf{b})$ is neither new nor special CWT, but merely just a result of sampling a subspace from the definition domain of $Y(\mathbf{a}, \mathbf{R}, \mathbf{b})$. This means that some information is just cropped by such a subsampling; in particular we may lose some information about elongated elliptic patterns in $f(\mathbf{x})$. But $Y(\mathbf{a}, \mathbf{R}, \mathbf{b})$ is a special case of the general definition $Y(\mathbf{A}, \mathbf{b})$ rather than argument sampling, because it is restricted to a special subfamily of wavelets. In that case the associated reduction of degrees of freedom appeared as a natural consequence of restricting the ψ . This did not trigger any additional information loss, i.e. the use of (1) instead of (9) does not recover any new information if ψ is radially symmetric.

3.2. Inverting the multidimensional CWT

Further on, we will deal mainly with the entirely isotropic case. The CWT is easily invertible in such a case, and the inversion formula reads

$$f(\mathbf{x}) = \frac{1}{C_{\psi\gamma}} \int_0^\infty \frac{da}{a^{2n+1}} \int_{\mathbb{R}^n} Y(a, \mathbf{b}) \gamma \left(\frac{|\mathbf{x} - \mathbf{b}|}{a} \right) d\mathbf{b}$$

$$= \frac{1}{C_{\psi\gamma}} \int_0^\infty \kappa^{n-1} d\kappa \int_{\mathbb{R}^n} \Upsilon(\kappa, \mathbf{c}) \gamma (|\kappa \mathbf{x} + \mathbf{c}|) d\mathbf{c},$$

$$C_{\psi\gamma} = \int_0^\infty \hat{\gamma}(s) \hat{\psi}^*(s) \frac{ds}{s} = \frac{1}{S_n} \int_{\mathbb{R}^n} \hat{\gamma}(s) \hat{\psi}^*(s) \frac{ds}{|s|^n}, \quad (11)$$

where $\gamma(t)$ is a radially-symmetric ‘reconstruction kernel’, which can differ from ψ in general, while $\hat{\gamma}$ and $\hat{\psi}$ are the corresponding Fourier images. The constant S_n is the surface area of a unit sphere in \mathbb{R}^n .

The formula (11) represents a minor generalization of the one given e.g. by Wang and Lu (2010), but involving an arbitrary number of dimensions and arbitrary γ . We could not find a reference for this more general case, so we provide a brief derivation of (11) in the Appendix A. We also provide there a discussion of some subtleties concerning the correct understanding and practical use of this inversion formula (they also appear important in the 1D case).

It seems that in more complicated cases the CWT can be inverted too, though the inversion formula attains even more degrees of freedom. However, we do not consider such general cases below.

In (11), the Fourier transforms $\hat{\psi}$ and $\hat{\gamma}$ are radially symmetric functions themselves, and they may be expressed by a single-dimensional Hankel transform:

$$\hat{\psi}(s) = \hat{\psi}(s) = \frac{(2\pi)^{\frac{n}{2}}}{s^{\frac{n}{2}-1}} \int_0^\infty \psi(t) J_{\frac{n}{2}-1}(st) t^{\frac{n}{2}} dt. \quad (12)$$

For $n = 2$, this simplifies to

$$\hat{\psi}(s) = 2\pi \int_0^\infty \psi(t) J_0(st) t dt. \quad (13)$$

The integral for $C_{\psi\gamma}$ requires that $\hat{\gamma}(0)\hat{\psi}(0) = 0$, or the CWT cannot be inverted using this reconstruction kernel. This condition represents the mutual admissibility requirement for γ and ψ . At least one of these functions should integrate to zero, i.e. to have a vanishing first momentum (this appears entirely analogous to the 1D case).

3.3. Importance of the orthogonality of the wavelet basis

How the wavelet transform (10) and its inversion (11) are interrelated and why we use different kernel functions ψ and γ ?

By combining (10) and (11) and noting that it should hold for any input function f , we may obtain a symbolic orthogonality relation:

$$\int_0^\infty \frac{da}{a^{2n+1}} \int \gamma \left(\frac{|\mathbf{x} - \mathbf{b}|}{a} \right) \psi \left(\frac{|\mathbf{x}' - \mathbf{b}|}{a} \right) d\mathbf{b} = C_{\psi\gamma} \delta(\mathbf{x}' - \mathbf{x}). \quad (14)$$

Of course, this equality is sensible only if $C_{\psi\gamma}$ is neither zero nor infinity.

In particular, if $\gamma \equiv \psi$ then we must require $C_{\psi\psi} < +\infty$, which is also known as the admissibility condition on ψ . In this case the wavelet ψ would form an orthogonal basis, viewed in the (a, \mathbf{b}) space. In fact, mathematically it might be more convenient to use the same kernel ψ in the both formulae, thus dealing solely with orthogonal bases in the Hilbert space.

But in practice we usually apply the following transformation sequence:

$$f(\mathbf{x}) \xrightarrow{\text{CWT}} Y(a, \mathbf{b}) \xrightarrow{\text{noise thresholding}} Y_{\text{thr}}(a, \mathbf{b}) \xrightarrow{\text{CWT}^{-1}} \tilde{f}(\mathbf{x}). \quad (15)$$

Here, the noise thresholding stage mixes all the deal because Y_{thr} is no longer a wavelet transform at all (notice that an arbitrary function of a and \mathbf{b} is not necessarily a valid wavelet transform of any $f(\mathbf{x})$). Therefore, the inversion formula plays even more important role that it might seem: it should intelligently find such an $\tilde{f}(\mathbf{x})$ which has a wavelet transform \tilde{Y} close to Y_{thr} . Since (11) is a linear operator than it represents, basically, a projection in the Hilbert space. It is not difficult to show that with $\gamma = \psi$ we deal with an orthogonal projection minimizing the L_2 norm of $|\tilde{Y} - Y_{\text{thr}}|$. However, such a minimizing is not necessarily useful in practice: in our case it might be more useful to minimize the noise that appears in \tilde{f} through the noisy Y_{thr} (and coming, after all, from the input sample $\{x_i\}$). Then it might appear reasonable to use a different kernel γ , and (11) then describes an oblique projection rather than orthogonal one.

But playing with γ in such a way we may achieve quite intriguing conclusions. Formally, from (11) it follows that we can even adopt ψ to be just a Gaussian or other bell-shaped smoothing kernel, rather than a wavelet with vanishing first momentum, and then use a wavelet-like shape for γ . Mathematically, the inversion formula works if $\int \gamma = 0$, but $\int \psi \neq 0$. Hence, even just a simple smoothing transform can be easily inverted, if we assume an appropriate γ in (11). One may ask then: why we actually need wavelets and the CWT? Why not to use this more simple setting with Gaussian ψ , thus trying to decompose $f(\mathbf{x})$ into a set of Gaussian components of different scale and position?

However, such a setting does not appear practical exactly because the orthogonality of such a Gaussian basis is lost. In this case it appears that different resolutions (i.e., different a -slices in $Y(a, \mathbf{b})$ function) become severely dependent. Basically, if ψ is merely a Gaussian then any large-scale slice of $Y(a, \mathbf{b})$ represents just a smoothed version of the small-scale ones. Since all resolution layers become interdependent, such an analysis would not be a truly multiresolution one. Or, in other words, this means that our decomposition into elementary Gaussians would lack uniqueness: we can easily approximate a wide Gaussian by a superposition of more narrow Gaussians, disregarding the large-scale part. Thus, multiple resolutions are no longer informative in this case.

In particular, applying in (15) a noise-filtering procedure to $Y(a, \mathbf{b})$ would be rather meaningless in this case: masking out some piece of the (a, \mathbf{b}) -space from $Y(a, \mathbf{b})$ would not completely remove the associated pattern in the original function $f(\mathbf{x})$. Moreover, after applying (10) to the ‘denoised’ $\tilde{f}(\mathbf{x})$, the noisy pattern might even restore in $Y(a, \mathbf{b})$, as if it was not masked.

Therefore, even though we may use an ‘oblique’ inversion formula with $\gamma \neq \psi$ for some practical noise-control purposes, for our goals it is necessary that the ‘orthogonal’ inversion formula with $\gamma = \psi$ at least exists, i.e. that $C_{\psi\psi}$ is finite. This would mean that $\tilde{f}(\mathbf{x})$ can be represented (at least in theory) as a superposition of the wavelets ψ having different scale and position, although for practical reasons we may build \tilde{f} by using another kernel γ .

3.4. Informal justification of the method via the smoothed Laplace operator

Let $\varphi(\mathbf{t})$ is a smoothing kernel, or bell-like shape in n dimensions. Put

$$\psi(\mathbf{t}) = \Delta\varphi(\mathbf{t}) = \sum_{i=1}^n \frac{\partial^2 \varphi}{\partial t_i^2}. \quad (16)$$

Then, integrating (4) by parts,

$$Y(\mathbf{A}, \mathbf{b}) = (\mathbf{A}\mathbf{A}^T) \cdot \int f''(\mathbf{x}) \varphi(\mathbf{A}^{-1}(\mathbf{x} - \mathbf{b})) d\mathbf{x}. \quad (17)$$

Here $f''(\mathbf{x})$ is an $n \times n$ Hessian matrix, and dot \cdot stands for the scalar product of two matrices of equal size.

For a radially symmetric generating function,

$$\varphi(t) = \varphi(t) \implies \psi(t) = \psi(t) = \varphi''(t) + \frac{n-1}{t}\varphi'(t), \quad (18)$$

we obtain

$$Y(\mathbf{a}, \mathbf{R}, \mathbf{b}) = (\mathbf{R}^T \mathbf{D}^{-1} \mathbf{R}) \cdot \int f''(\mathbf{x}) \varphi\left(\left|\frac{\mathbf{R}(\mathbf{x} - \mathbf{b})}{\mathbf{a}}\right|\right) d\mathbf{x}. \quad (19)$$

For the entirely isotropic case,

$$\begin{aligned} Y(\mathbf{a}, \mathbf{b}) &= a^2 \int \Delta f(\mathbf{x}) \varphi\left(\frac{|\mathbf{x} - \mathbf{b}|}{a}\right) d\mathbf{x} \\ &= a^{n+2} \int \Delta f(\mathbf{b} + a\mathbf{t}) \varphi(t) dt. \end{aligned} \quad (20)$$

The last formula attains the most intuitive interpretation: the wavelet transform of $f(\mathbf{x})$ is equivalent to smoothing the Laplacian of $f(\mathbf{x})$ with the kernel φ . For example, for small a we have $Y(\mathbf{a}, \mathbf{b}) \simeq a^{n+2} \Delta f(\mathbf{b})$, if φ is normalized to have a unit integral.

The Laplacian Δf , in one of its equivalent definitions, determines how much the function changes, in average, if we move by a small step in a random direction:

$$\Delta f(\mathbf{x}_0) = \lim_{r \rightarrow 0} \frac{2n}{r^2} \left(\frac{1}{\sigma(S_r)} \int_{S_r(\mathbf{x}_0)} f(\mathbf{x}) d\sigma(\mathbf{x}) - f(\mathbf{x}_0) \right). \quad (21)$$

Here, $S_r(\mathbf{x}_0)$ is a sphere of a small radius r around \mathbf{x}_0 , and $d\sigma$ is its surface integration measure. Positive $\Delta f(\mathbf{x}_0)$ means that $f(\mathbf{x})$ grows in average, if we step by a small quantity from \mathbf{x}_0 . If simultaneously Δf is large, this likely indicates that we are near a local minimum of $f(\mathbf{x})$, or at least inside a local concavity (considered relatively to the local tangent plane). Negative Δf , if it is large in absolute value, likely indicates a local maximum of $f(\mathbf{x})$ or at least a local convexity relative to the tangent plane.

Therefore, if we select ψ to be the Laplacian of some smoothing kernel φ , the resulting CWT would highlight possible local inhomogeneities: either p.d.f. leaks (or gaps) or p.d.f. peaks (clumps of objects). It is important that all these inhomogeneities are always considered relatively to some local large-scale background (tangent plane at \mathbf{x}_0). Therefore, it is not a big issue if a subtle statistical

subfamily is polluted by e.g. a large-scale underlying gradient of $f(\mathbf{x})$. Even if the local maximum associated to such a subfamily is distorted by the gradient so heavily that it no longer represents a local maximum in the strict meaning, it still appears as a local convexity with the same $\Delta f(\mathbf{x}_0)$. The wavelet ψ is blind to linear components, so it will ‘see’ only that local convexity, filtering out any underlying background.

However, we note that Laplacian Δf in $n > 1$ dimensions is a less rigorous tool than f'' for $n = 1$. In two or more dimensions the single condition $\Delta f < 0$ is not yet enough to ensure that we are inside a local convexity, and hence to rigorously claim the detection of a statistical clump. The condition $\Delta f < 0$ only means that f is decreasing *in average* whenever we step aside, but not necessarily decreasing when stepping *in either* direction. In other words, near a saddle point Δf can be negative too, but this does not yet imply the existence of a local convexity and hence of a clump. However, we expect that in practice such cases can be easily identified on the CWT visually, so investigation of just the Laplacian Δf may be informative enough.

For the Gaussian φ and $n = 2$, we obtain the famous 2D MHAT wavelet:

$$\varphi(t) = e^{-\frac{t^2}{2}} \implies \psi(t) = (t^2 - 2)e^{-\frac{t^2}{2}}. \quad (22)$$

Based on what was said above, computing the isotropic CWT based on the 2D MHAT wavelet is equivalent to Gaussian smoothing of the Laplacian $\Delta f(\mathbf{x})$.

4. Statistical estimations of the CWT and patterns detection

4.1. Estimating the 2D wavelet transform from a random sample

This part of the analysis method remains essentially the same as in the 1D case, but we nonetheless need to reproduce its basic formulae. Assume that we aim to analyse the distribution of a random quantity x , and this x has the p.d.f. of $f(x)$, or ‘the x -distribution’. As in the 1D case, the CWT (1) can be viewed as the mathematical expectation of another random quantity y :

$$y = \psi(\mathbf{A}^{-1}(\mathbf{x} - \mathbf{b})), \quad Y(\mathbf{A}, \mathbf{b}) = \mathbb{E}y. \quad (23)$$

For each point in the space of the (\mathbf{A}, \mathbf{b}) arguments, this quantity generates the so-called ‘y-distribution’.

We use the same shorthand $\langle * \rangle$ for the sample-averaging operation:

$$\langle \phi \rangle := \frac{1}{N} \sum_{i=1}^N \phi_i \quad \text{or} \quad \langle \phi(x) \rangle := \frac{1}{N} \sum_{i=1}^N \phi(x_i). \quad (24)$$

Then, the natural estimation of Y is the sample mean of y_i :

$$\tilde{Y}(\mathbf{A}, \mathbf{b}) = \langle y \rangle = \langle \psi(\mathbf{A}^{-1}(\mathbf{x} - \mathbf{b})) \rangle, \quad (25)$$

or the sample wavelet transform (SWT). It is an unbiased and for large N asymptotically Gaussian estimate of Y . Its variance is

$$\begin{aligned} D &:= \mathbb{D} \tilde{Y} = \frac{\mathbb{D} y}{N} = \\ &= \frac{1}{N} \left[\int_{-\infty}^{+\infty} f(x) \psi^2(\mathbf{A}^{-1}(\mathbf{x} - \mathbf{b})) dx - Y^2 \right], \quad (26) \end{aligned}$$

and it can be estimated by the classic unbiased variance estimate

$$\tilde{D} = \frac{\langle y^2 \rangle - \langle y \rangle^2}{N - 1}. \quad (27)$$

Finally, our primary goodness-of-fit statistic represents the standardized version of \tilde{Y} . Let our null hypothesis be expressed as $Y(\mathbf{A}, \mathbf{b}) = Y_0(\mathbf{A}, \mathbf{b})$. Then,

$$z(\mathbf{A}, \mathbf{b}) = \frac{\tilde{Y}(\mathbf{A}, \mathbf{b}) - Y_0(\mathbf{A}, \mathbf{b})}{\sqrt{\tilde{D}(\mathbf{A}, \mathbf{b})}} \quad (28)$$

represents our primary test statistic. As before, it is nothing more than just the Student t-statistic for the sample $\{y_i\}$. Large values of z indicate that at the given point (\mathbf{A}, \mathbf{b}) , our null hypothesis failed to model the sample, meaning that there is a statistically significant pattern with these scale and position.

4.2. Computing 2D CWT significance levels in the approximation of Gaussian noise

As in the 1D framework, we attempt to test the following hypotheses:

$$\begin{aligned} H_0 &: Y(\mathbf{A}, \mathbf{b}) = Y_0(\mathbf{A}, \mathbf{b}) \text{ everywhere in } \mathcal{D}, \\ H_A &: Y(\mathbf{A}, \mathbf{b}) \neq Y_0(\mathbf{A}, \mathbf{b}) \text{ somewhere in } \mathcal{D}, \quad (29) \end{aligned}$$

where \mathcal{D} is some predefined domain in the (\mathbf{A}, \mathbf{b}) space, e.g. the Gaussian domain.

The H_0/Y_0 is rejected if the following occurs:

$$z_{\max} > z_{\text{thr}}, \quad z_{\max} = \max_{(\mathbf{A}, \mathbf{b}) \in \mathcal{D}} |z(\mathbf{A}, \mathbf{b})|. \quad (30)$$

A notice that z_{\max} is a random quantity here (an extreme value of the random field z). Basically, it is our test statistic. The critical significance level z_{thr} is determined based on the distribution function of z_{\max} :

$$P_{\max}(z) = \Pr(z_{\max} < z | H_0). \quad (31)$$

The threshold level z_{thr} depends on the desired false alarm probability (FAP) as $\text{FAP} = 1 - P_{\max}(z_{\text{thr}})$. Or, alternatively, we can derive the FAP based on the observed z_{\max} , and then the associated significance (Baluev and Shaidulin, 2018).

To accomplish this testing procedure, we must derive the extreme value distribution (EVD), $P_{\max}(z)$, for the random field $z(\mathbf{A}, \mathbf{b})$. As in the 1D case, we derive this distribution analytically, assuming that $z(\mathbf{A}, \mathbf{b})$ is standard Gaussian inside \mathcal{D} , and applying the so-called Rice method (Azaïs and Delmas, 2002). Here we again rely on the intermediary theory from (Baluev, 2013).

We do not discuss the details of this theory, but we note that the Rice method allows one to derive an efficient analytic approximation to $P_{\max}(z)$, for a Gaussian or even non-Gaussian random process or field. The Rice approximation works asymptotically for $z \rightarrow \infty$, i.e. for the more practical small FAP values. Simultaneously, such an approximation appears to limit the FAP from the upper side. The latter property is very important, because it means that this method never increases the fraction of false alarms: even if the Rice approximation appeared inaccurate, the actual FAP value may be only smaller, so any features detected in the CWT would remain significant. Given this, we recognize that because of high task complexity the formulae presented below neglect some secondary terms of the Rice approximation (in particular, those related to the extrema attained on the boundary of \mathcal{D}). So the upper-limit property might appear formally broken from the mathematical point of view. Also, it might appear broken if we take into account the non-Gaussian deviations of z . However, simulation tests (see Sect. 8)

revealed that in practically reasonable ranges this property remains satisfied, confirming that the neglected terms keep small.

In fact, all necessary formulae can be easily derived from the 1D case with only minor changes to the formulae, replacing a two-dimensional Gaussian random field by the three-dimensional one. We consider here only the case of entirely isotropic CWT, which implies a 3-dimensional random field $z(a, \mathbf{b})$.

The one-sided false alarm probability is then given by

$$\text{FAP}^+(z) \sim A_0 \left(\frac{z^2}{2} + 1 \right) e^{-\frac{z^2}{2}} + A_1 e^{-\frac{z^2}{2}}, \quad (32)$$

This is a special case of formula (20) from (Baluev, 2013). In this work we keep only the primary term in (32), assuming z is large. Then we obtain:

$$\text{FAP}^+(z) \sim W_{00} z^2 e^{-\frac{z^2}{2}}, \quad (33)$$

where $W_{00} = A_0/2$ is given by

$$W_{00} = \frac{1}{4\pi^2} \int_{\mathcal{D}} \sqrt{\det \mathbf{G}(a, \mathbf{b})} da d\mathbf{b}, \quad \mathbf{G} = \text{Var } z', \quad (34)$$

The matrix \mathbf{G} in the last formula represents the covariance matrix of the 3-dim gradient z' . It can be asymptotically approximated as in the 1D case:

$$\lim_{N \rightarrow \infty} G_{ij} = \frac{\text{Cov}(y'_i, y'_j)}{\mathbb{D}y} - \frac{\text{Cov}(y, y'_i) \text{Cov}(y, y'_j)}{(\mathbb{D}y)^2}, \quad (35)$$

where the index denotes the differentiation variable, either a or one of the \mathbf{b} components.

In practical computations, we do not know the covariances appearing in (35), because they depend on the unknown p.d.f. $f(\mathbf{x})$ which we aim to analyse. However, we may replace them by the corresponding sample estimates:

$$\begin{aligned} \text{Cov}(y'_i, y'_j) &\simeq \langle y'_i y'_j \rangle - \langle y'_i \rangle \langle y'_j \rangle, \\ \text{Cov}(y, y'_i) &\simeq \langle y y'_i \rangle - \langle y \rangle \langle y'_i \rangle, \\ \mathbb{D}y &\simeq \langle y^2 \rangle - \langle y \rangle^2. \end{aligned} \quad (36)$$

The formulae (35) and (36) allow us to compute an estimate $\widehat{\mathbf{G}}$ that we can substitute in (34) in place of \mathbf{G} and then integrate it numerically. This substitution infers a relative error of $\sim 1/\sqrt{N}$ in the result.

Finally, to treat the two-sided estimation FAP we must double (33):

$$\text{FAP}(z) \sim 2W_{00} z^2 e^{-\frac{z^2}{2}}. \quad (37)$$

4.3. Determining the Gaussian domain in the 2D CWT

As noticed above, individual values of the statistic z are asymptotically standard normal for $N \rightarrow \infty$, if the null hypothesis Y_0 is true. Hence, z is an asymptotically Gaussian random field. However, for a finite N there are always points in the (a, \mathbf{b}) space, where the normality is broken too much. In particular, the normality is always violated at small enough a , where the wavelets become so narrow-localized that we have just a few or even one term dominating in the sum (25). In general, we can determine some limited ‘normality domain’ \mathcal{D} , depending on N , such that inside \mathcal{D} the random field z is close to being Gaussian, but essentially non-Gaussian outside. To determine \mathcal{D} we need to define some reasonable normality indicators.

As in the 1D case, the first rough indicator of the normality is the effective number of terms contributing to the sum (25). It can be roughly estimated by:

$$n(\mathbf{A}, \mathbf{b}) = \left[\sum_{i=1}^N \varphi(\mathbf{A}^{-1}(\mathbf{x} - \mathbf{b})) \right] \left/ \int_{-\infty}^{+\infty} \varphi(x) dx \right. . \quad (38)$$

Since φ has approximately the same localization as ψ , the number of terms dominating in (38) is approximately the same as in (25), but now all these terms are positive and do not cancel.

We also tried to follow a more rigorous method to construct the normality indicator, based on the Edgeworth-type decomposition of the FAP. This method is detailed in (Baluev, 2018). It remains almost unchanged here, but now the dimension of the gradient z' is increased from 2 to 3, while the dimension of the Hessian matrix z'' becomes 3×3 with 6 independent elements. Therefore, the total dimension of the random vector (z, z', z'') , which plays the central role in this method, is increased from 6 to 10. Unfortunately this apparently moderate increase of dimensionality triggered a huge increase of algebraic complexity of the task, so we could not replicate the derivation even with the help of computer al-

gebra. We only give here a reduced result, which appeared to convolve to a simple final form regardless of a complicated derivation. The asymptotic distribution of the one-sided false alarm probability appears to have the following double-series shape:

$$\begin{aligned} \text{FAP}^\pm(z) &\sim z^2 e^{-z^2} \times \left[(W_{00} + \mathcal{O}(z^{-2}) + \dots) \pm \right. \\ &\quad \pm \frac{z^3}{\sqrt{N}} (W_{1,-3} + \mathcal{O}(z^{-2}) + \dots) + \\ &\quad \left. + \mathcal{O}\left(\frac{z^6}{N}\right) + \dots \right], \\ W_{ij} &= \frac{1}{(2\pi)^2} \int_{\mathcal{D}} q_{ij}(a, \mathbf{b}) \sqrt{\det \mathbf{G}(a, \mathbf{b})} da d\mathbf{b}. \end{aligned} \quad (39)$$

Basically it remained the same as in the 1D case, except for the change z to z^2 in the very first factor. The first part of the sum that does not involve N , represents the Gaussian part, while the rest is a non-Gaussian perturbation. Here we left just one leading term in each series decomposition, so we only have the primary 'Gaussian' coefficient W_{00} , which has $q_{00} = 1$, and the first-order non-Gaussian correction with $W_{1,-3}$, defined via the quantity $q_{1,-3}(a, \mathbf{b})$. The latter appears to have the same form as in the 1D case:

$$q_{1,-3} = -\frac{1}{3} \text{As } y, \quad (40)$$

where $\text{As } y$ is the skewness of the y -distribution. In practice, $\text{As } y$ in (40) can be estimated simultaneously with the SWT (25) and matrix \mathbf{G} in (35), using the sample skewness of y_i .

As in the 1D case, we do not recommend the use of (39) directly because of its likely poor convergence, and because we actually have just one correction term there. Instead, we may use this formula to remove the points (a, \mathbf{b}) that contribute too much in the cumulative non-Gaussian term.

Namely, let us rewrite (39) as

$$\begin{aligned} \text{FAP}^\pm(z) &= \int_{\mathcal{D}} \mu(z, a, \mathbf{b}) da d\mathbf{b}, \quad \mu = \mu_{\text{gauss}} + \mu_{\text{nongauss}}, \\ \mu_{\text{gauss}} &\simeq \frac{z^2 e^{-z^2}}{(2\pi)^2} \sqrt{\det \mathbf{G}}, \quad \frac{\mu_{\text{nongauss}}}{\mu_{\text{gauss}}} \sim \pm \frac{z^3}{\sqrt{N}} q_{1,-3}. \end{aligned} \quad (41)$$

Now, if we restrict the domain \mathcal{D} to only such points where

$$\left| \frac{\mu_{\text{nongauss}}}{\mu_{\text{gauss}}} \right| \leq \varepsilon \quad (42)$$

then we will have $|\text{FAP}_{\text{nongauss}}| \leq \varepsilon \text{FAP}_{\text{gauss}}$, i.e. the relative magnitude of the non-Gaussian error in the FAP is bounded by the same threshold ε .

Therefore, the necessary normality criterion can be formulated as follows:

$$\frac{z_*^3}{\sqrt{N}} |q_{1,-3}(a, \mathbf{b})| < \varepsilon, \quad (43)$$

which represents a reduced version of a similar criterion for the 1D case.

The meaning of this z_* in (43) is the maximum z -level, for which the normality will be guaranteedly preserved with the desired accuracy.¹ This z_* may be derived from the desired smallest considerable FAP level FAP_* as $\text{FAP}_* = \text{FAP}_{\text{gauss}}(z_*)$. It therefore depends on many input parameters (including W_{00}), but nonetheless it appears relatively insensitive to all them, thanks to roughly logarithmic dependence with respect to FAP_* . In the 1D case we recommended to put $z_* \sim 3$ in practice, while in the 2D case a bit more safe value $z_* \sim 4-6$ may be used.

Another parameter ε sets the desired limit on the relative magnitude of possible non-Gaussian corrections to the FAP at $z = z_*$. We usually set $\varepsilon^2 = 0.1$. Using these parameters, the normality domain in the 1D case appeared generally close to the one obtained from the simplistic criterion $n(a, \mathbf{b}) \geq n_{\min}$ with $n_{\min} = 10$.

Since we neglected in (43) several additional terms, this criterion can be simplified to the following shape:

$$|\text{As } y| < \frac{3\varepsilon}{z_*^3} \sqrt{N} = \frac{\sqrt{N}}{\text{const}}, \quad \text{const} \sim 100 - 300. \quad (44)$$

Here, $\text{As } y$ can be estimated from y_i by the corresponding sample momentum.

As in the 1D case, the skewness $\text{As } y$ plays a predominant role here. It determines the non-Gaussian

¹It is typical that relative magnitude of a non-Gaussian error in a density function grows infinitely in the tails. Therefore, we have to limit z by some z_* , below which we expect to constrain the non-Gaussianity.

error of the largest order. Therefore, we can suppress the non-Gaussianity and simultaneously significantly expand the domain \mathcal{D} if we select such a wavelet ψ that implies a reduced $\mathbb{A}y$.

Here we need to discuss a yet another subtle statistical issue missed in the 1D paper. Given the formulae above, the domain \mathcal{D} is determined based on the input sample $\{x_i\}$, and as such it may not be considered as an *a priori predefined* domain. As a general rule, it might be a bad and potentially dangerous practice to replace an *a priori* information required by a statistical test with an *a posteriori* estimate instead. Such a substitution may lead to unexpected statistical biases sometimes, since it violates the conditions of the original statistical test. However, the domain determined by (43) is a sample-based *approximation* to some ‘theoretic’ normality domain \mathcal{D} that does not depend on individual x_i in the input sample. The relative error of this approximation should remain small, corresponding to the typical statistical error $\sim 1/\sqrt{N}$. Therefore, the effect of random x_i on the derived \mathcal{D} (and hence — on the coefficient W_{00}) is in this case negligible, and this \mathcal{D} mainly depends on the actual p.d.f. $f(\mathbf{x})$, on the wavelet ψ , and on the sample size N .

5. Deriving optimal minimum-noise wavelets

5.1. 2D wavelets normalization

The generating function must satisfy the following restrictions:

$$\begin{aligned} \varphi(t) &> 0 \text{ everywhere,} & \varphi(t) &= \varphi(-t), \\ \varphi'(t) &> 0 \text{ for } t < 0, & \varphi'(t) &< 0 \text{ for } t > 0. \end{aligned} \quad (45)$$

These conditions define some domain Π in the functional space. Notice that the condition $\varphi(t) > 0$ is a bit excessive here, because if $\varphi'(t) < 0$ is satisfied for $t > 0$ then it is enough to require that $\varphi(t) > 0$ for just $t \rightarrow \infty$. The positiveness of φ for all other t then follows automatically.

Similarly to the 1D case, to legally compare different wavelets between each other, we formulate the following normalization constraints:

$$\int_0^{+\infty} \varphi(t) t dt = \frac{1}{2\pi}, \quad \int_0^{+\infty} \psi^2(t) t dt = \frac{1}{2\pi}. \quad (46)$$

The first of the equalities (46) naturally requires φ to be a normalized smoothing kernel, so that the CWT always has the same magnitude and dimension as $\Delta f(\mathbf{x})$. This sets a ‘standard’ signal normalization in the CWT. As in the 1D case, the second equation of (46) fixes a ‘standard’ noise normalization in the SWT, namely it fixes the magnitude of $D(a, \mathbf{b})$ given a small scale a .

An arbitrary wavelet $\psi = \Delta\varphi$ can be forced to fulfill (46) by the following affine transformation:

$$\begin{aligned} \varphi_{\text{norm}}(t) &= K\varphi(kt), \\ \psi_{\text{norm}}(t) &= Kk^2\psi(kt), \\ K &= (2\pi)^{-\frac{2}{3}} \left(\int_0^{+\infty} \varphi t dt \right)^{-\frac{1}{3}} \left(\int_0^{+\infty} \psi^2 t dt \right)^{-\frac{1}{3}}, \\ k &= (2\pi)^{\frac{1}{6}} \left(\int_0^{+\infty} \varphi t dt \right)^{\frac{1}{3}} \left(\int_0^{+\infty} \psi^2 t dt \right)^{-\frac{1}{6}}. \end{aligned} \quad (47)$$

In particular, for the 2D MHAT wavelet we obtain:

$$\text{2DMHAT : } \quad K = 0.2936839, \quad k = 1.358407. \quad (48)$$

5.2. Finding optimal 2D wavelet

Analogously to the 1D case, for small a the skewness of the y -distribution becomes approximated by

$$\mathbb{A}y \approx \frac{\mathcal{R}}{\sqrt{a^2 f(\mathbf{b})}}, \quad (49)$$

where

$$\mathcal{R} = 2\pi \int_0^{+\infty} \psi_{\text{norm}}^3(t) t dt. \quad (50)$$

Therefore, $\mathbb{A}y$ is drastically reduced if the following condition is satisfied:

$$\int_0^{+\infty} \psi^3(t) t dt = 0. \quad (51)$$

This is not fulfilled by the 2D MHAT which has $\mathcal{R} \approx -0.64$. In the 1D case, we had the analogous proportionality coefficient $\mathcal{R} = -0.49$, so matters are getting worse in 2D.

If the normalization (46) is satisfied, the objective functional to minimize for optimality becomes:

$$a^6 \det \mathbf{G} \approx T(\psi) = \left(2\pi \int_0^{+\infty} \psi'^2 t^3 dt - 1 \right) \left(\pi \int_0^{+\infty} \psi'^2 t dt \right)^2. \quad (52)$$

This approximation is obtained analogously to the 1D case, by assuming that a is small and $f(\mathbf{x})$ is constant within the wavelet localization domain.

The minimization of (52) allows to minimize the coefficient W_{00} (34) in the FAP representation (33), assuming that the domain \mathcal{D} is fixed.

An arbitrary input wavelet must be first transformed to the appropriate scales using (47), and then the resulting ψ_{norm} should substituted to $T(\psi)$. This yields us the following objective functional:

$$T_{\text{norm}} = \frac{(2\pi)^{\frac{2}{3}}}{4} \left(\int_0^{+\infty} \psi'^2 t^3 dt - \int_0^{+\infty} \psi^2 t dt \right) \left(\int_0^{+\infty} \varphi t dt \right)^{\frac{4}{3}} \times \left(\int_0^{+\infty} \psi^2 t dt \right)^{-\frac{11}{3}} \left(\int_0^{+\infty} \psi'^2 t dt \right)^2. \quad (53)$$

From (34) and (52), the coefficient W_{00} becomes

$$W_{00} \approx \frac{1}{4\pi^2} \int_{\mathcal{D}} \sqrt{T_{\text{norm}}} \frac{dad\mathbf{b}}{a^3}, \quad (54)$$

so in practice the values of $\mathcal{W} = \sqrt{T_{\text{norm}}}/(2\pi)^2$ might have perhaps a more intuitive interpretation than T_{norm} itself. Namely, we have $W_{00} \simeq \mathcal{W} \text{Vol}(\mathcal{D})$, where $\text{Vol}(\mathcal{D})$ is the total volume of the domain \mathcal{D} , considered in the space of $(\log a, \mathbf{c})$, but without the large-scale part $a \gtrsim \mathbb{D}x$, where the approximation (52) does not work (as numeric tests confirmed, this large-scale portion in W_{00} is usually negligible).

The scale-invariant quantity \mathcal{W} describes how noisy a particular wavelet is. For example, the 2D MHAT wavelet has $\mathcal{W} = 0.12$, which means very low noise. However, this low noise level is achieved by the cost of a large noise skewness, which is not acceptable in this work.

Since all integrals above involve the integration measure $t dt = d(t^2/2)$, it is now convenient to use

$u = t^2/2$ as an auxiliary proxy variable:

$$\begin{aligned} \varphi(t) &= \tilde{\varphi}\left(\frac{t^2}{2}\right), & \psi(t) &= \tilde{\psi}\left(\frac{t^2}{2}\right), \\ \tilde{\psi}(u) &= 2u\tilde{\varphi}''(u) + 2\tilde{\varphi}'(u). \end{aligned} \quad (55)$$

Now, the parametric wavelet model from (Baluev, 2018) can be rewritten as:

$$\begin{aligned} \tilde{\varphi}(u) &= P(u)e^{-u}, & P(u) &= p_0 + p_1u + \dots + p_mu^m, \\ \tilde{\varphi}'(u) &= P_1(u)e^{-u}, & P_1(u) &= P'(u) - P(u), \\ \tilde{\varphi}''(u) &= P_2(u)e^{-u}, & P_2(u) &= P_1'(u) - P_1(u), \\ \tilde{\psi}(u) &= P_{\Delta}(u)e^{-u} & P_{\Delta}(u) &= 2uP_2(u) + 2P_1(u). \end{aligned} \quad (56)$$

Substituting this model to T_{norm} yields an algebraic objective function in p_k , and another algebraic equality constraint follows from (51). We need to find such p_k that minimize the objective conditionally to the constraint. This optimization task can be solved using the Lagrange multipliers approach.

However, the polynomial $P(u)$ cannot be arbitrary. Since $\varphi(t)$ should belong to the domain Π defined in (45), the following equivalent restrictions must be satisfied:

$$P(u) > 0 \text{ for } u \rightarrow +\infty, \quad P_1(u) < 0 \text{ for } u > 0. \quad (57)$$

Assuming without loss of generality that $p_m = +1$, this guarantees $P(u) > 0$ and $P_1(u) < 0$ for large u . Then the constraints can be reformulated equivalently as just

$$P_1(u) \text{ has no real roots for } u > 0. \quad (58)$$

We must discard all local optima outside of the domain Π , i.e. all solutions $\{p_k\}$ for which $P_1(u)$ has positive real roots.

But it is also necessary to verify possible boundary optima. The boundary of Π can be mathematically determined by violating (58) in a way to obtain a transitional state. Condition ‘the polynomial has no positive real roots’ can be violated so in two ways. The first one is to require that $u = 0$ is a root, equivalent to setting the free term of P_1 to zero, or setting $p_1 = p_0$. The second way is a bit more tricky. Since we need to trigger just a boundary state, we may request that ‘the polynomial has double or multiple roots’, which includes all occurrences whenever

a new pair of roots is about to appear (possibly, but not necessarily, at $u > 0$). This is equivalent to equating the P_1 discriminant $D(p_1, \dots, p_m)$ to zero, therefore defining an extra algebraic equality constraint in terms of $\{p_k\}$. Not all occurrences with $D = 0$ necessarily indicate the boundary of Π , because e.g. the emerging double root u may be negative, which does not imply any violation in (58), or we could already have other roots $u > 0$ and thus are already well outside of the domain Π . But regardless of that, the nonlinear subspace $D = 0$ necessarily includes the boundary of Π , so we can just seek all optima in this subspace, then post-check whether they are actually located at the boundary, and if yes whether they supply a smaller minimum of T_{norm} than any local minimum already found in the domain interior. This will complete the comprehensive search of optimal solutions in Π .

We performed a comprehensive search of wavelets represented by the model (56) for $m = 1$ and $m = 2$, but we surprisingly found none at least satisfying (51) and (45) simultaneously. The cases $m = 3$ and $m = 4$ are too difficult to be processed analytically, even with computer algebra, but extensive numeric search also did not reveal any wavelet at least satisfying the constraints, so we could not even start the search for optimality. This contrasts with the 1D case from (Baluev, 2018), where we did find the necessary optimal wavelet already for $m = 2$.

In order to acquire a more deep understanding of the issue, we considered the model of another type:

$$\varphi(t) = e^{-|t|^p}, \quad p > 0. \quad (59)$$

Here, parameter p regulates the wings of the generating function: larger p , more abruptly they decrease to zero. We found that the condition (51) is then satisfied for $p = 6.34$. We additionally calculated that in the 1D case this condition is satisfied for a considerably smaller degree $p = 3.26$. That is, the 2D case likely requires the tails of φ to be almost twice as abrupt as in the 1D case. Consequently, the kernel part of φ must be relatively wider in 2D.

Sadly, unskewed models of this type are unpleasantly more noisy, e.g. we had $\mathcal{W} = 2.17$ for the $p = 6.34$ 2D solution. To a certain extent, an increase of \mathcal{W} seems to be a necessary sacrifice paid

for the vanishing noise skewness. Note that non-Gaussian noise is poorly predictable and difficult to model, even if it has a smaller overall magnitude, so we put more priority on reducing its deviation from the normality.

Since in the 1D case we could find a suitable wavelet using the model with square-exponent tails, $\exp(-t^2)$, in the 2D case we likely need a quart-exponent law, $\exp(-t^4)$. This means that $\exp(-u)$ in (56) should be replaced by something like $\exp(-u^2)$. The search using such parametric model for $m = 2$ successfully resulted in the following wavelet:

$$\begin{aligned} \tilde{\varphi}(u) &= (2.73050 - 1.00854u + u^2)e^{-\frac{u^2}{2}}, \\ \tilde{\psi}(u) &= (-2.01708 - 2.92199u + 8.06833u^2 - \\ &\quad - 6.53900u^3 - 2.01708u^4 + 2u^5)e^{-\frac{u^2}{2}}, \\ K &= 0.0796646, \quad k = 1.35480. \end{aligned} \quad (60)$$

It has $\mathcal{W} = 1.07$. Below we will refer it as ‘2DOPT1’ wavelet.

However, functions involving $\exp(-t^4)$ did not appear to have an easy analytic form of the Fourier transform. So we continued to seek yet another wavelet with a more practical functional form.

We should consider symmetric φ that have depressed tails, i.e. zero skewness and decreased kurtosis (speaking as if φ was a p.d.f.). Among the general class of Pearson distributions, only the type II family satisfies this constraint. This is basically the family of symmetric beta distribution, or ‘powers of semi-circle’. If φ is such a symmetric beta distribution, put

$$\tilde{\varphi}_\nu(u) = (1 - u)^\nu, \quad u \leq 1, \quad \nu \geq 0. \quad (61)$$

Then from (13) we derive the Fourier transform

$$\begin{aligned} \hat{\varphi}_\nu(s) &= 2\pi \int_0^{\sqrt{2}} \left(1 - \frac{t^2}{2}\right)^\nu J_0(st) t dt = \\ &= 2\pi\Gamma(\nu + 1) \left(\frac{\sqrt{2}}{s}\right)^{\nu+1} J_{\nu+1}(s\sqrt{2}), \end{aligned} \quad (62)$$

which behaves closely to the usual bell-like shape (with only negligible wavy oscillations in the tails). Note that the last equality was suggested by the machine computer algebra, so we do not provide its

derivation. For $\nu \rightarrow \infty$ we come to the Gaussian φ and 2D MHAT ψ , which is too much skewed in terms of (51). But for $\nu = 2$ we have such ψ that (51) is remarkably satisfied. Unfortunately, this simple special case is still unsuitable for us, because such ψ has jumps at $t = \pm 1$, hence the derivative ψ' is singular and the objective T_{nrn} becomes infinite.

Therefore, we may seek the suitable wavelet in the following parametric form, constructed analogously to the Gaussian case:

$$\begin{aligned}\tilde{\varphi}(u) &= (1-u)^\nu P(u), \\ P(u) &= p_0 + p_1 u + \dots + p_m u^m, \\ \tilde{\varphi}'(u) &= (1-u)^{\nu-1} P_1(u), \\ P_1(u) &= (1-u)P'(u) - \nu P(u), \\ \tilde{\varphi}''(u) &= (1-u)^{\nu-2} P_2(u), \\ P_2(u) &= (1-u)P_1'(u) - (\nu-1)P_1(u), \\ \tilde{\psi}(u) &= (1-u)^{\nu-2} P_\Delta(u), \\ P_\Delta(u) &= 2uP_2(u) + 2(1-u)P_1(u),\end{aligned}\quad (63)$$

where $u \in [0, 1]$. Now we optimize against p_k and ν simultaneously (ν is not necessarily an integer). Note that although the definition (61) required $n \geq 0$, the quantity T_{nrn} is defined and finite only if $\nu > \frac{5}{2}$.

Using this parametric form, we found the first optimal solution already for $m = 1$: $\nu = 2.98010$ with $p_0 = 0.397808$ and $p_1 = 1$. This optimum is located very close to the boundary of Π , but still in the interior. However, it corresponds to $\mathcal{W} = 1.83$ which is still too large for us, e.g. the wavelet (60) is less noisy.

The next optimal solution was obtained for $m = 2$. It corresponds to the following wavelet:

$$\begin{aligned}\tilde{\varphi}(u) &= (0.141826 + 0.330025u + u^2)(1-u)^\nu = \\ &= 1.471851(1-u)^\nu - 2.330025(1-u)^{\nu+1} + \\ &\quad + (1-u)^{\nu+2}, \\ \tilde{\psi}(u) &= (-0.584764 + 3.452872u - 40.719896u^2 + \\ &\quad + 81.626277u^3)(1-u)^{\nu-2} = \\ &= 43.774488(1-u)^{\nu-2} - 166.891909(1-u)^{\nu-1} + \\ &\quad + 204.158934(1-u)^\nu - 81.626277(1-u)^{\nu+1}, \\ \nu &= 4.388516, \quad u \leq 1, \\ K &= 1.54811, \quad k = 0.652500.\end{aligned}\quad (64)$$

Below we will refer it as ‘2DOPT2’ wavelet. It has $\mathcal{W} = 1.05$, which is almost the same as for 2DOPT1.

The graphical shape of (64) is also almost identical to (60), so numerically they appear to be practically the same wavelets. However, the functional shape of (64) is more analytically tractable in the Fourier space.

Since we obtained almost the same shape using two different functional models, we believe that further improvement of T_{nrn} is not very likely, if we do not violate some natural restrictions of smoothness and good convergence, or the normality condition (51). It looks as if $\mathcal{W} \approx 1$ was a natural lower limit on possible noise in the 2D SWT.

5.3. Finding optimal reconstruction kernel

Entirely analogously to the 1D case, we may obtain that the variance of the estimated density $\tilde{f}(x)$, obtained by applying the inversion formula (A.1) in some finite ‘signal domain’ \mathcal{S} , is

$$N \mathbb{D} \tilde{f}(x) \simeq f(x) \int_{\mathbb{R}^n} R_{\mathcal{S}}^2(x, x') dx', \quad (65)$$

where

$$R_{\mathcal{S}}(x, x') = \frac{1}{C_{\psi\gamma}} \iint_{\mathcal{S}} \psi\left(\frac{x-b}{a}\right) \gamma\left(\frac{x-b}{a}\right) \frac{dad\mathbf{b}}{a^{2n+1}}. \quad (66)$$

The cumulative relative variance characteristic then becomes:

$$N \int_{\mathbb{R}^n} \frac{\mathbb{D} \tilde{f}(x)}{f(x)} dx \simeq \iint_{\mathbb{R}^n \times \mathbb{R}^n} R_{\mathcal{S}}^2(x, x') dx dx'. \quad (67)$$

We therefore should minimize the L_2 norm $\|R_{\mathcal{S}}\|$ with respect to γ to obtain the least noisy p.d.f. reconstruction:

$$\|R_{\mathcal{S}}\|^2 = \iint_{\mathbb{R}^n \times \mathbb{R}^n} R_{\mathcal{S}}^2(x, x') dx dx' \mapsto \min_{\gamma} \quad (68)$$

Note that the effect of the domain \mathcal{S} is crucial here, because e.g. if \mathcal{S} spans the entire (a, \mathbf{b}) space then $R_{\infty} = \delta(x - x')$ thanks to the wavelet orthogonality, and the variance $\mathbb{D} \tilde{f}$ gets therefore infinite. This reflects the known fact that p.d.f. estimation based on a finite sample is an ill-posed task: we must cut off at least small scales in (11) to obtain a meaningful reconstruction (or we just ‘reconstruct’ the input

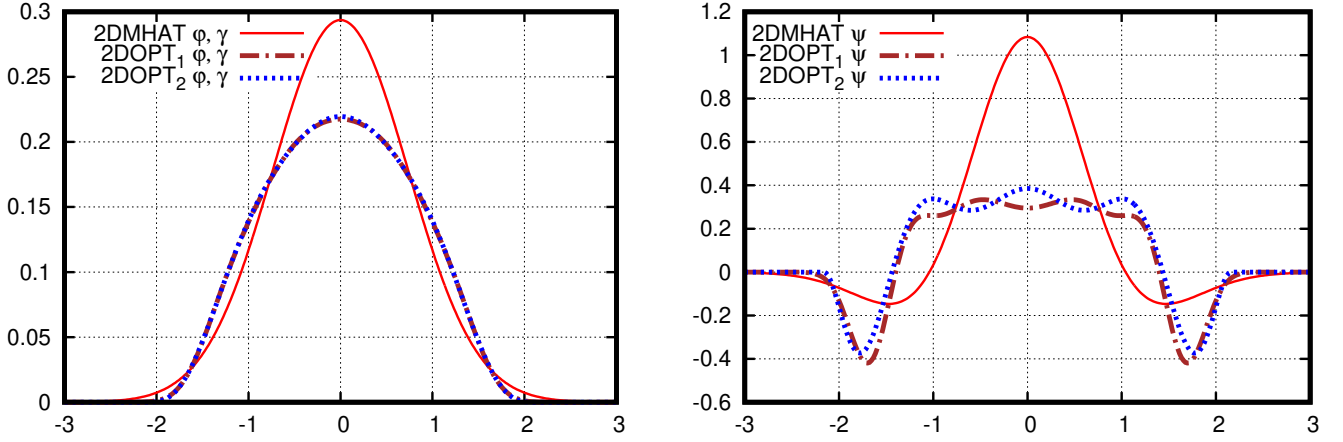


Figure 1: Radial functions for two optimal 2D wavelets (ψ) and for their generators (φ), compared with ψ and φ of the classic 2D MHAT wavelet. In the 2D case, the optimal generating function γ coincides with $-\varphi$. Everything shown after the normalization (46).

sample as a comb of delta functions, rather than any smooth p.d.f.).

As in the 1D case, we consider the optimality in the local sense, i.e. we optimize each infinitesimal contribution to $\mathbb{D}\tilde{f}$ that comes from a small vicinity around some (a_0, \mathbf{b}_0) . In this case, the integral (66) is approximated by just the naked integrand:

$$R_S(\mathbf{x}, \mathbf{x}') \propto \frac{1}{C_{\psi\gamma}} \psi\left(\frac{\mathbf{x} - \mathbf{b}}{a}\right) \gamma\left(\frac{\mathbf{x}' - \mathbf{b}}{a}\right) \Rightarrow \\ \Rightarrow \|R_S\| \propto \frac{\|\gamma\|}{|C_{\psi\gamma}|}, \quad (69)$$

where the omitted all coefficients that do not depend on γ .

$C_{\psi\gamma}$ is basically a scalar product of two functions, $\hat{\psi}(s)/s^n$ and $\hat{\gamma}(s)$:

$$C_{\psi\gamma} = \int_0^{+\infty} \frac{\hat{\psi}^*(s)}{s^n} \hat{\gamma}(s) s^{n-1} ds = \frac{1}{S_n} \int_{\mathbb{R}^n} \frac{\hat{\psi}^*(s)}{|s|^n} \hat{\gamma}(s) ds, \quad (70)$$

By the Plancherel theorem, this scalar product can be equivalently determined by an integral in the \mathbf{t} -space, operating on the corresponding Fourier originals. Therefore, to minimize $\|R_S\|^2$ with respect to γ , we must maximize the ratio $(\hat{\psi}/s^n, \hat{\gamma})^2 / \|\hat{\gamma}\|^2$. Since this ratio is a cosine-angle type quantity, the obvious maximum is achieved for

$$\hat{\gamma}(s) \propto s^{-n} \hat{\psi}(s) = -s^{2-n} \hat{\varphi}(s), \quad s \geq 0. \quad (71)$$

Here we used the property that applying the Laplace operator to some $\varphi(\mathbf{t})$ is equivalent to multiplying $\hat{\varphi}(s)$ by $-|s|^2$ in the Fourier s -space.

From (71) one can derive a remarkable result: in the 2D case ($n = 2$) the optimal reconstruction kernel coincides with the negated generating function, $\gamma(\mathbf{t}) \equiv -\varphi(\mathbf{t})$.

If γ is computed from (71) without any additional coefficients then the inversion constant in (11) becomes

$$C_{\psi\gamma} = \int_0^{+\infty} |\hat{\varphi}(s)|^2 s^{3-n} ds = \frac{1}{S_n} \int_{\mathbb{R}^n} |\hat{\gamma}(s)|^2 ds. \quad (72)$$

This is basically the L_2 norm of γ , or its total Fourier power.

When computing such an integral for a linear mixture $\varphi = \sum_\nu c_\nu \varphi_\nu$, where φ_ν are defined via (61), one may utilize the following useful identity:

$$\int_0^{+\infty} \hat{\varphi}_\nu(s) \hat{\varphi}_\mu(s) s ds = \frac{4\pi^2}{1 + \nu + \mu}, \quad (73)$$

which assumes $n = 2$.

The general model (56) is not used here, but for the 2DMHAT case it is easy to obtain $C_{\psi\gamma} = 2\pi^2$.

In addition it is necessary to take into account the normalization scaling (47), which implies $\gamma_{\text{norm}}(\mathbf{t}) = Kk^{2-n}\gamma(k\mathbf{t})$ and requires $C_{\psi\gamma}$ to be scaled up by $K^2 k^{4-3n}$.

In particular, for the classic 2DMHAT and for our new 2DOPT2 wavelet, the result is

$$\begin{aligned} \text{2DMHAT} : \quad C_{\psi\gamma} &= 0.922636, \\ \text{2DOPT2} : \quad C_{\psi\gamma} &= 0.875171. \end{aligned} \quad (74)$$

Summarizing this section, we note that this method of finding an optimal reconstruction kernel seemingly works only for $n = 1$, $n = 2$, and possibly for $n = 3$. Already for $n = 3$ we obtain a singular Fourier image $\hat{\gamma} = \hat{\varphi}/s$, which looks rather impractical, though probably still tractable mathematically. But for $n = 4$ and above, the constant $C_{\psi\gamma}$ becomes infinite in (72). Therefore, the cases of higher dimensions still need a more careful investigation.

6. Reconstruction of the p.d.f. after wavelet denoising

We adopt the same method of the p.d.f. reconstruction as we used in the 1D case. This is basically the matching pursuit algorithm, intended to model the p.d.f. $f(x)$ in the most economic way, still agreeing with the significance threshold, that is avoiding (30) in the normality domain \mathcal{D} . This is based on an iterative application of noise filtering based on (30) and application of the inversion formula (11), until no significant structures are left in \mathcal{D} .

This means that all the steps (15) are iterated until the following condition is satisfied:

$$\max_{\mathcal{D}} |z(a, \mathbf{b})| \leq z_{\text{thr}}. \quad (75)$$

Hence, we basically solve a type of a nonlinear programming task considering the L_∞ norm of z as a constraint, while some implicit simplicity measure of Y as an objective function. The latter objective can be formulated as to minimize the number of nonzero wavelet coefficients that contribute to \tilde{f} via (11), so in some sense this might be treated as an L_0 norm in the (a, \mathbf{b}) -space (Hara et al., 2017). That is, we try to obtain the simplest model of f still satisfying the noise significance limits.

In fact, any other combination of L_p norms is possible here, e.g. McEwen et al. (2017) used a χ^2 metric in place of (75), so this implies the L_2 norm. Each combination of norms may have its own advantages or disadvantages, but this discussion is out of the scope of this paper.

More details of this inversion method are already given in (Baluev, 2018) and discussed in (Baluev and Shaidulin, 2018), and here we only generalize it to the 2D case in an obvious manner.

The associated computation complexity is, of course, significantly larger in the 2D case. Unfortunately, current implementation of this part is relatively impractical: processing of the asteroid test case presented below was possible only with a top-class multi-cpu system. One possible solution to further soften the ‘dimensionality curse’ and achieve a practically feasible code might be to integrate (11) by using the Monte Carlo approach or by applying genetic algorithms, instead of relying on an inefficient regular grid. However, we did not assess or implement this option yet.

In any case, we emphasize that the reconstruction of the p.d.f. is not the main goal of our analysis. It carries more demonstrative purpose, while the most important part is the detection of significant patterns in the CWT, i.e. the detection of structures that passes the threshold (30).

7. The updated code: improved 1D and new 2D algorithm

The C++ code with a command-line analysis pipeline is available for download at <https://sourceforge.net/projects/waveletstat>.

This package now contains algorithms for the both 1D and 2D analysis. The 1D code published with the previous paper, is now considerably revised and improved. The changes were worked out after a year of practical application and tests of the code. They include the following.

1. The computing speed was improved a lot, thanks to optimizations of the algorithm itself, as well to an efficient parallelization, based on the C++11 multithreading tools (the previous version was only partly parallelized). We also optimized the code in such a way that it is now capable to handle large samples that involve $\sim 10^5$ of objects and above (like e.g. asteroid databases).
2. Output files were optimized for size. Previously, the file with a wavelet transform could

grow extremely huge (e.g. ~ 10 Gb and beyond). Now we revised its format by removing unnecessary debug-like information, portions outside of the Gaussian domain, and values below some ‘compression’ threshold (it can be quite a mild, e.g. $z = 1$ allows for a quite efficient compression). The resulting file size was reduced by the factor of $\sim 100 - 1000$, depending on the parameters.

3. Now user can select hard as well as soft thresholding when reconstructing the p.d.f. (previously only the soft thresholding was available). The hard thresholding appears considerably faster thanks to a smaller number of matching pursuit iterations, though soft thresholding results in a more smooth p.d.f. model.
4. The algorithm may now adopt three types of the initial p.d.f.: constant zero (an improper distribution with infinite variance), flat in a specified analysis range, and Gaussian which mean and variance are estimated from the sample. Previously only the zero initial p.d.f. was allowed. The Gaussian model allows to adaptively incorporate most of the large-scale p.d.f. structure, avoiding reconstructing it by iterations. Hence, the p.d.f. reconstruction process runs faster, since only the small-scale details are iterated. The formula used to compute the CWT of a Gaussian or of a flat distribution are given in Appendix B. The flat model is natural for angular variables (in the 1D case). This is an alternative (and possibly more justified) approach than the workaround used by Baluev and Shaidulin (2018), which was based on sample cloning to get rid of the p.d.f. jumps near the segment endpoints.
5. The normality domain \mathcal{D} is now considered differently at small scales ($a < \mathbb{D}x$) and at large scales ($a > \mathbb{D}x$). In the small-scale zone we require the following conditions to be satisfied for a given point (a, \mathbf{b}) : (i) number of sample points x_i within the wavelet cut-off domain (see below) is at least 4, (ii) the quantity $n(a, \mathbf{b})$ is at least 1, (iii) the variance estimate $\widetilde{D}(a, \mathbf{b})$ is non-zero, and finally (iv) the primary normality criterion (43), or its 1D-case version from (Baluev, 2018), is satisfied. The first

three additional conditions were necessary to workaround several technical issues revealed in the practical application of the algorithm with practical data. In the large-scale zone, we require that (i) $\widetilde{D}(a, \mathbf{b})$ is non-zero, and (ii) $n(a, \mathbf{b})$ is above $n_{\text{thr}} = \varepsilon^{-2}$, typically 10 (small n indicates a small number statistic). Such a special treatment of the large-scale zone appeared because in practice the normality test (43) is often failed at large scales, but nonetheless the values of the z statistic are always large there, so this non-Gaussianity is usually unrelated to the effect of small-sample statistic and does not indicate that the corresponding CWT values are insignificant. The large-scale zone contains information about only a global structure of $f(\mathbf{x})$, for example about its unit normalization. Although this global-scale structure usually is not very interesting in itself, it is still important to accurately reconstruct it. Therefore, we decided not to use (43) at large scales.

6. The normality domain determined in accordance with the instructions above is further postprocessed to remove the extremely porous structure of its boundary at small scales. In the 1D case, we purge away all the points in the (a, b) -plane that were formally classified as Gaussian, but appear isolated (surrounded by non-Gaussian points at the neighbouring b), or if the continuous segment formed by Gaussian points is too short along the b -axis (shorter than $0.3a$). All such isolated points or too short point sequences are reclassified as non-Gaussian. This allowed to make the Gaussian/non-Gaussian transition boundary more regular, hence to reduce the size of the output and of the associated figure files. In the 2D case, we apply a more intricate algorithm based on a disk-kernel dilation of the non-Gaussian domain in the \mathbf{b} -plane, followed by a similar dilation of the remaining Gaussian domain. This resulted in the removal of all Gaussian pieces that could not embed a disk of a given size². The radius of the disk is set so that its area appears equal to $0.3a^2$.

²This method was inspired by the ‘morphol-

7. It appeared that the previous version of the code missed many of the terms that should appear in the normality test (hidden inside $q_{1,-1}$ and $q_{2,-6}$), due to a programming bug. Now we fixed it, although this fortunately did not have practical consequences on the results, because the missed terms appeared negligible in our tests. Notice that in the 2D version of the algorithm all the terms $q_{2,j}$ for any j , as well as all $q_{1,j}$ with $j > -3$, are neglected in any case. This error significantly affected only the coefficient W_{02} , especially for the WAVE2 wavelet in the 1D case. However, this term contributes to the FAP with a small factor z^{-2} , so it usually remains small. In the 2D case, the coefficient W_{02} is neglected at all.
8. Another potentially important mistake in the legacy code appeared when estimating various sample momenta by the corresponding sample averages. For example, the sample-based estimator for the covariance $\lambda_{XY} = \text{Cov}(X, Y)$ is

$$l_{XY} = \frac{1}{N} \sum_{i=1}^N (X_i - l_X)(Y_i - l_Y),$$

$$l_X = \frac{1}{N} \sum_{i=1}^N X_i, \quad l_Y = \frac{1}{N} \sum_{i=1}^N Y_i. \quad (76)$$

In practice the quantities X and Y are related to the wavelet ψ or to its derivatives, computed in the point $(x - b)/a$. Since all such functions are well-localized, with exponential tails in the 1D case, we optimized the code by neglecting in (76) all the quantities for which $|(x - b)/a|$ is above some limit. Denoting such reduced sum by \sum' , and the number of the non-negligible terms by N' , this would result in:

$$l_{XY} \approx \frac{1}{N} \sum' (X_i - l_X)(Y_i - l_Y) + \frac{N - N'}{N} l_X l_Y,$$

$$l_X \approx \frac{1}{N} \sum' X_i, \quad l_Y \approx \frac{1}{N} \sum' Y_i. \quad (77)$$

ogy' operator of the `IMAGEMAGICK` utility. See the associated web page for further explanation, <http://www.imagemagick.org/Usage/morphology/>. Our approach is equivalent to applying the 'Open' method with a 'Disk' kernel.

However, in the old version of the code the second term of (77), containing $l_X l_Y$, was mistakenly missed. Fortunately, this term is only important at large scales, because otherwise the reduced sum \sum' contains relatively few terms. Then l_X and l_Y become small quantities of the order N'/N , and so is $l_X l_Y$. So the missed addition $l_X l_Y$ has the relative magnitude of $\sim N^{-1}$. A similar mistake appeared in the momenta of the third degree:

$$l_{XYZ} = \frac{1}{N} \sum_{i=1}^N (X_i - l_X)(Y_i - l_Y)(Z_i - l_Z)$$

$$\approx \frac{1}{N} \sum' (X_i - l_X)(Y_i - l_Y)(Z_i - l_Z)$$

$$- \frac{N - N'}{N} l_X l_Y l_Z, \quad (78)$$

where the last term was again missed in the old code. However, here it has the relative magnitude of just N^{-2} . Analogously, for the quad-degree momenta l_{XYZT} the corresponding addition would be about N^{-3} relatively to the total sum. After fixing this bug, we did not notice any visible changes in practical tests.

9. The published algorithm now involves a 2D version, which uses all the theory described above. However, the 2D version may be still be considered as beta, since it got smaller amount of testing. The code is organized universally in the sense that the 1D and 2D algorithms are produced by the same source files, just compiled with different parameters. In the future such code organization may help us to extend the algorithms to even larger dimensions.

Now let us give some more details concerning the computation algorithm that we omitted in (Baluev, 2018). First of all, it takes the following input.

1. The input sample $\{x_i\}$.
2. The desired wavelet (4 wavelets available in the 1D case, and 2 in the 2D case).
3. The desired shift range $[b_{\min}, b_{\max}]$, or the corresponding square domain in the 2D case (also determined by just b_{\min} and b_{\max}).
4. The scale range $[a_{\min}, a_{\max}]$, where a_{\min} must be a small positive value, but a_{\max} can be infi-

nite, which would mean $\kappa_{\min} = 0$. The reasonable value of a_{\min} depends, in general, on the sample size N (larger N means smaller a_{\min}) and on the peaky parts of $f(x)$ (where x_i are sampled more densely, hence the most small scales can be reached). However, we cannot give any mathematically definite formula for a_{\min} , so this parameter needs to be guessed by the user or determined by experimenting. Reducing a_{\min} would slow the computation down, but increasing a_{\min} too much would result in the lost CWT structures. Usually there is some ‘safe’ a_{\min} that could allow to discover all significant structures in the (a, b) -space (below this a_{\min} all values of $z(a, b)$ are smaller than the noise threshold).

5. The adimensional parameter h that defines the resolution of various grids. Basically, it has the meaning of how fine we intend to sample $\psi(t)$.
6. Other fine-tuning options, in particular the type of the initial p.d.f. approximation Y_0 .

In the output, our algorithm first computes and saves the initial SWT and auxiliary data, namely $Y(a, b) - Y_0(a, b)$ and $z(a, b)$, the simplified normality indicator $n(a, b)$, and the logical (0/1) flag that indicates whether the full normality test was passed or not. Some additional more detailed output can be requested if necessary.

On the second phase, the algorithm reconstructs the p.d.f. model by matching pursuit iterations, and filtering out all points that fail the significance test for $|z(a, b)|$. This is done simultaneously for three probabilistic levels: FAP = 31% (or 1-sigma level), FAP = 4.6% (or 2-sigma level), and FAP = 0.27% (or 3-sigma level). In the end, the reconstructed p.d.f. models corresponding to these three tolerance levels is saved, as well as the corresponding residual SWTs (so that the user can verify that no significant structures were left in the (a, b) -plane after the iterations). This second phase takes usually considerably longer time that just to compute the SWT. The matching pursuit iteration are continued until the volume of the domain where (75) is violated, is reduced to 0.3 in the small-scale zone and 0.5 in the large-scale zone, or until 100 iterations are made.

The algorithm involves several optimizations, in

particular it keeps only such terms in the summation (25), and similar summations, for which the argument of $\psi(t)$ appeared below some maximum radius. This basically cuts away the tails of $\psi(t)$, removing negligible values from the summations. A similar cutting is applied when integrating (11) with the reconstruction kernel $\gamma(t)$. In the case of 2DOPT2 wavelet there is a natural limit on t , where $\psi(t)$ vanishes by definition. In the 1D case, the limit is selected to be 5 – 7, depending on the wavelet.

The sampling of the SWT with respect to the parameter b can be linear or logarithmic, depending on the user request. In the latter case, we basically analyse the variable $\log b$ instead of b , and regarding the initial linear b , the scale a attains the meaning of the relative scale.

With respect to the parameter a , the SWT is always sampled using a special non-linear scaling. It is such that the following quantity appears sampled linearly (i.e., equidistantly):

$$l(a) = \log\left(1 + \frac{\sigma}{a}\right) = \log(1 + \sigma\kappa), \quad (79)$$

where σ is the input sample variance. This formula was motivated by our intention to sample local peaks of the SWT approximately uniformly everywhere in the domain \mathcal{D} . From the formula (54) and from the behavior of individual components in the gradient z' , it follows that the local peaks of $z(a, b)$ should have approximately constant width in terms of the variables $\log a$ (for small a) and c . The logarithmic natural scaling for a also follows if we consider the integral autocorrelation function for $\psi((b - x)/a)$ with different a and b : it depends on the difference of $c = -b/a$ and on the *ratio* of the scales a . But for large a we face a degeneracy, so a more reasonable variable becomes $\kappa = 1/a$. Therefore, the nonlinear parametrization (79) appeared as the mixture of the two scales.

Our algorithm contains two major phases: the computation of the SWT $Y(a, b)$, and the iterative reconstruction of the denoised p.d.f. $f(x)$, using the inversion formula (11). The second phase can be switched off by setting an appropriate command argument. In this case, the algorithm will not only process faster, but also use a considerably smaller amount of memory, since it does not need to store the entire CWT array.

The computational complexity of the first phase, as implemented in our algorithm, can be roughly expressed by a formula

$$N_\psi \sim h^{-n-1}NL^n\Delta l, \quad (80)$$

where N_ψ is the number of wavelet evaluations, n is the dimension (1 or 2), h is an adimensional grid resolution parameter (about 0.03 to 0.1), N is the input sample size, L is an adimensional localization range of the wavelet (depending on the wavelet, varies from ~ 4 to ~ 10), and l depends on the requested scale range $[a_{\min}, a_{\max}]$:

$$\Delta l = l(a_{\min}) - l(a_{\max}). \quad (81)$$

If $a_{\max} = \infty$ (which is a valid value actually meaning $\kappa_{\min} = 0$), this Δl turns into just $\log(1 + \sigma/a_{\min})$. Remarkably, N_ψ does not depend on $f(x)$ or on the requested range of the b parameter.

The second phase is iterative, and each iterations contain (i) the inversion of the thresholded SWT and (ii) an update of the CWT comparison model Y_0 . The complexity of the first part is roughly expressed as

$$N_\gamma \sim h^{-2n-1} \left(\frac{BL}{a_{\min}} \right)^n \Delta l S_z, \quad (82)$$

where N_γ is the number of evaluations of $\gamma(t)$, B is the range of the b parameter requested by user (in the 1D case), or the side of the corresponding square (in the 2D case). The complexity also depends on the fraction S_z of the statistically significant values of z -statistic that remained at the current iteration. This is because insignificant values do not contribute in the result ($S_z \ll 1$ usually). Remarkably, N_γ does not depend on $f(x)$ or on the input sample size N directly, though small N would imply that reasonable a_{\min} is likely large.

The second part of the second phase is equivalent to computing an integral over n dimensions, for parameters covering a grid in $n + 1$ dimensions. Taking into account all the optimizations, this corresponds to the following numeric complexity:

$$N_\psi \sim h^{-2n-1} \left(\frac{BL}{a_{\min}} \right)^n \Delta l. \quad (83)$$

Compared to (82), this part of the algorithm does not profit from the small factor S_z . Basically, it just

plainly applies the CWT to the current model of $f(x)$. Further on, this can be optimized by using the information that we should update the CWT in only a small domain surrounding the ‘significant’ part of the (a, b) -grid, because changes in the ‘insignificant’ part should be mostly negligible (thanks to the wavelet orthogonality). This would allow to add the factor S_z to (83). However this is still a work to do.

As we can see, the p.d.f. reconstruction phase of the algorithm currently has rather poor efficiency, especially for $n = 2$, so it needs to be optimized further to become more practical. But concerning the case $n = 1$, both phases of our algorithm appear practically feasible, even for very large samples containing $N \sim 10^6$ objects.

Further technical details can be found in the readme file supplied with the code.

8. Practical tests and examples

8.1. Monte Carlo tests of the significance levels

Approximating the false alarm probability was one of the most complicated and possibly vulnerable part of the method. Therefore, we performed Monte Carlo simulations to verify that the relevant formulae is adequate and works as expected.

However, our simulations could only be limited, because the computing the CWT on a 3D grid is a practically hard task. Moreover, we had to increase the size of the simulated sample from $N \sim 1000$ (in 1D) to $N \sim 10000$ (in 2D), because otherwise the CWT would contain mainly the large-scale structure, which is not very interesting to test.

Therefore, the number of Monte Carlo trial was reduced to only 1000. In each trial we simulated a random sample, drawing it from the standard 2D Gaussian distribution, $\mathcal{N}_2(\mu = 0, \sigma^2 = 1)$. Then we computed the CWT, cutting all the scales below $a_{\min} = \sigma/\sqrt{N}$, and simultaneously determined the normality domain \mathcal{D} . Then we computed a pair of extreme values in \mathcal{D} :

$$z_{\max}^+ = \max_{\mathcal{D}} z(a, \mathbf{b}), \quad z_{\max}^- = \max_{\mathcal{D}} [-z(a, \mathbf{b})]. \quad (84)$$

To accurately compute these quantities, for each candidate extrema we applied a Newtonian iteration scheme in the 3D space (a, \mathbf{b}) . The necessary 3D

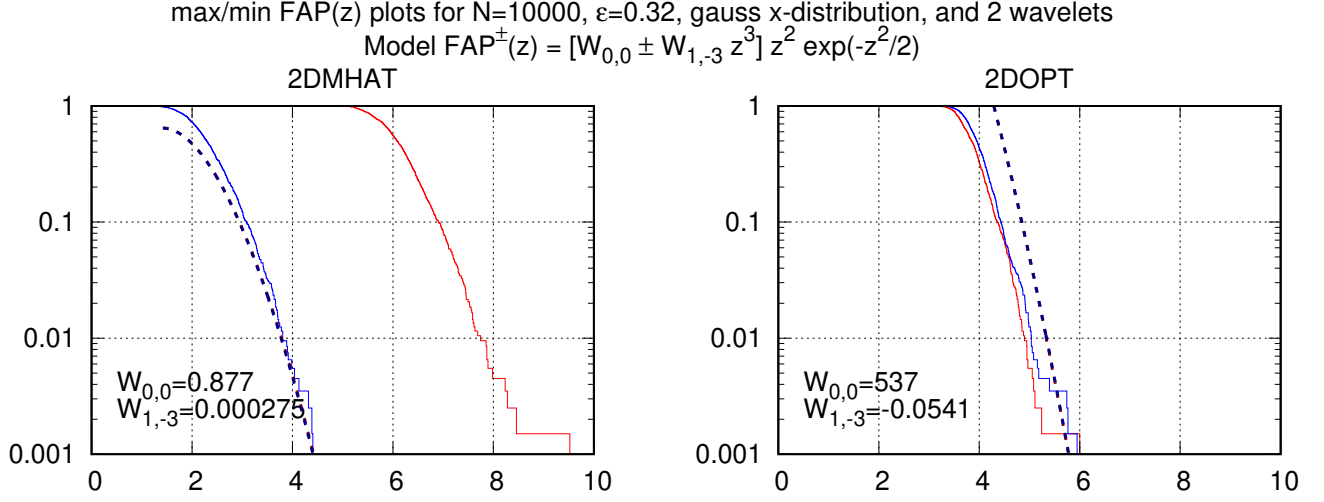


Figure 2: Analytic approximation (33), compared with Monte Carlo simulations. The simulations involved the normality criterion (43) and thus the coefficients W_{00} was restricted to the normality domain \mathcal{D} . Red-colored curves refer to positive extrema distributions (maxima of $z(a,b)$, FAP^+), while blue-colored ones are for the negative ones (minima of $z(a,b)$, FAP^-), though they appear mostly indistinguishable from each other. Theoretic approximations are shown in thicker dashed lines.

gradient and 3×3 Hessian matrix were computed simultaneously with z , using analytic formula (we omit them). This approach allowed us to reduce the computation time by rarifying the 3D grid, but without reducing the resulting values of z_{\max}^\pm .

The simulated extrema z_{\max}^\pm then were used to construct their empirical distribution functions and hence the simulated FAP curves. The latter were compared with the analytic approximations (33,39). This comparison is shown in Fig. 2. We can see that for the 2DOPT2 wavelet the agreement is good, i.e. our analytic formulae allow to determine z -threshold with a quite satisfactory accuracy. Moreover, we can see that the simulated distributions of z_{\max}^\pm almost coincide with each other, so this wavelet does not generate any significant skewness.

However, the 2D MHAT wavelet generated very small normality domain (indicated by small W_{00}). And even in this reduced domain the behaviour of z seems not quite Gaussian, because the distributions of z_{\max}^\pm appear pretty different from each other. This could appear because in the 2D case our normality test neglects several higher-order terms that likely work here (even if the skewness $\mathcal{A}_s y$ is formally suppressed). The analytic FAP approximation becomes expectedly poor in this case.

8.2. A practical test case: the 2D eccentricity distribution in the Main Belt

The 2D wavelet analysis is obviously more demanding, not only with respect to the required computing capabilities, but also with respect to the task and input data.

Let us consider a random sample of size N , distributed more or less uniformly in the n -dim cube having the side L . Then the average density of the points would be N/L^n , while the typical size of a volume containing just a single point would be $a_{\min} \sim LN^{-1/n}$. Therefore, volumes sized as $\sim a_{\min}$ or below would not be sampled adequately, so a_{\min} represents a natural smallest scale that can be analysed. In the 1D case we had $a_{\min} \sim L/N$, so it could be quite small for large samples. But now $a_{\min} \sim L/\sqrt{N}$, so even rather large samples do not allow to perform a fine-resolution analysis of the underlying p.d.f.

For example, having $N \sim 1000$ objects in our sample we cannot go below $a_{\min} \sim L/30$, where L is about sample variance. This is relatively moderate scale limit, compared to the 1D case, when we would have $a_{\min} \sim L/1000$ with the same N . Therefore, to reveal the full power of our method, we have to work with very large samples.

We opted to deal with the asteroid catalog

astorb.dat of the Lowell observatory.³ For our goals we selected only numbered asteroids, which gave us $N \sim 5 \times 10^5$. In theory, this would allow us to reach the scales as small as $a_{\min} \sim L/700$, which is comparable to $N = 700$ in the 1D case.

Since our analysis is isotropic, we need to select two physically and numerically comparable parameters. Initially we decided to use for this goal eccentric parameters ($e \cos \varpi, e \sin \varpi$), where e is orbital eccentricity of an asteroid, while ϖ is longitude of the perihelion. However, after some thinking we decided that the parameter ϖ is not entirely physical, because it is defined as a sum of two angles lying in different planes. We therefore stopped on the following pair of quantities:

$$\begin{aligned} f'_x &= \frac{ef_x}{\sqrt{f_x^2 + f_y^2}} &= e \cos \varpi', \\ f'_y &= \frac{ef_y}{\sqrt{f_x^2 + f_y^2}} &= e \sin \varpi', \end{aligned} \quad (85)$$

where f_x and f_y are Cartesian components of the Laplace vector. This is a vector of length e directed from the Sun to orbital perihelion, and based on the formulae of two-body motion (Kholshchevnikov and Titov, 2007) it can be expressed as follows:

$$\begin{aligned} \mathbf{f} = e\{ &\cos \omega \cos \Omega - \cos i \sin \omega \sin \Omega, \\ &\cos \omega \sin \Omega + \cos i \sin \omega \cos \Omega, \\ &\sin i \sin \omega \}, \end{aligned} \quad (86)$$

where ω is argument of the perihelion, Ω is the ascending node longitude, and i is orbital inclination.

Clearly, if i is small then $f'_x \simeq e \cos \varpi$ and $f'_y \simeq e \sin \varpi$, so we obtain almost what we initially aimed to obtain. However, for large i these f'_x and f'_y might be slightly different, representing in general the normalized projection of the Laplace vector on the ecliptic plane.

For these parameters we ran our software tool twice. In the first run, we obtained the CWT at a relatively high resolution $h = 0.05$ and with a small minimum scale $a_{\min} = 0.005$. We did not perform the p.d.f. reconstruction in this run, since it appeared

not feasible to complete even a single iteration. In the second run, we increased the grid step to $h = 0.1$ and the minimum scale to $a_{\min} = 0.01$. With these options we were capable to complete about 20 iterations of the p.d.f. reconstruction phase.

The results are plotted in Fig. 3. We represent the three-dimensional CWT as a series of 2D slices taken at different scales a . We plot a few of such slices in the figure, and a video movie showing our results in full is available in the electronic version of the paper following this figure. Also, the reconstructed p.d.f. model is shown in Fig. 4.

The color in the CWT plots encodes the normal quantile corresponding to the value of z in the given point (a, \mathbf{b}) , more explanation given by Baluev and Shaidulin (2018). Notice that the sign corresponds to the sign of Δf (after smoothing), so negative values mean a convex density function (e.g. near local maximum), while positive values mean concave p.d.f. (e.g. near local minimum). The hashed domain is where the normality test was failed.

We can see a fascinating evolution of arcing and ringing structures of different scale, position, and shape. Significant structures remain up to the smallest scales below $a \sim 0.01$, where we can see a small and accurate ring somewhat shifted from the center. The sign of z indicates a paucity of asteroids along this ring, so it might reflect e.g. some separatrix in the dynamical phase space (they usually represent sources of chaotic motion and thus are avoided). We unfortunately have to leave these results without any physical interpretation, since there is not enough space here. We only notice that wavelet analysis allows to reveal quite intriguing structures in the distribution, and these results need further investigation and assessment in subsequent works.

9. Conclusions

Our new version of the algorithm is suitable to analyse 2D distributions, thus it may be deemed as an improved analogue of the method presented by (Skuljan et al., 1999). Let us now highlight several main improvements of our wavelet analysis method in comparison with others:

1. We use a probabilistic detection criterion based on an asymptotic estimation of the p-

³See url <ftp://ftp.lowell.edu/pub/elgb/astorb.html>.

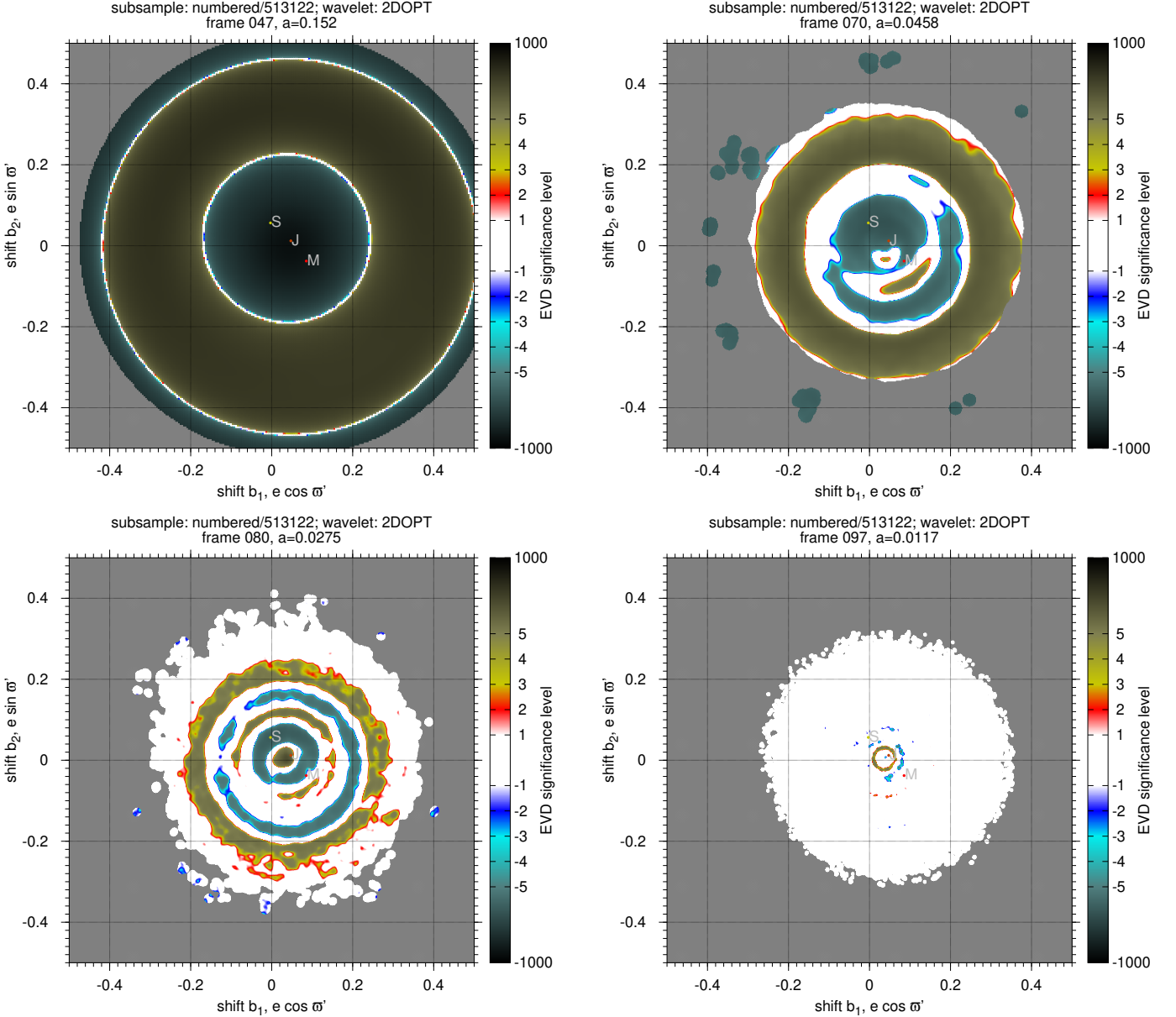


Figure 3: Several slices of the CWT for the 2D distribution of $(e \cos \varpi', e \sin \varpi')$ for the Main Belt asteroids. Slices correspond to several selected scales a , decreasing from 0.152 (approximately the sample variance) to ~ 0.01 . The color corresponds to the significance of the corresponding $z(a, \mathbf{b})$, as transformed to normal quantiles, with sign symbolically reflecting the sign of z . The hashed regions of each plot correspond to the non-Gaussian domain, where (43) was failed. In each frame we also label the position of Mars, Jupiter, and Saturn (the three main perturbers).

- value significance (false alarm probability), obtained with an adequate treatment of the ‘domain penalty’ effect. This approximation is practically accurate and entirely analytic, thus removing the need of Monte Carlo simulations.
2. We constructed an objective criterion to determine the suitable working domain in the shift-scale space, based on the Gaussianity require-

ment.

3. We derived optimal wavelets and optimal reconstruction kernels that allowed to improve the S/N ratio and to reduce the non-Gaussian deviations, thus expanding the working domain.

Among the limitations of our algorithm we may note that it is computationally demanding and hence rather slow. This cannot be avoided to a certain ex-

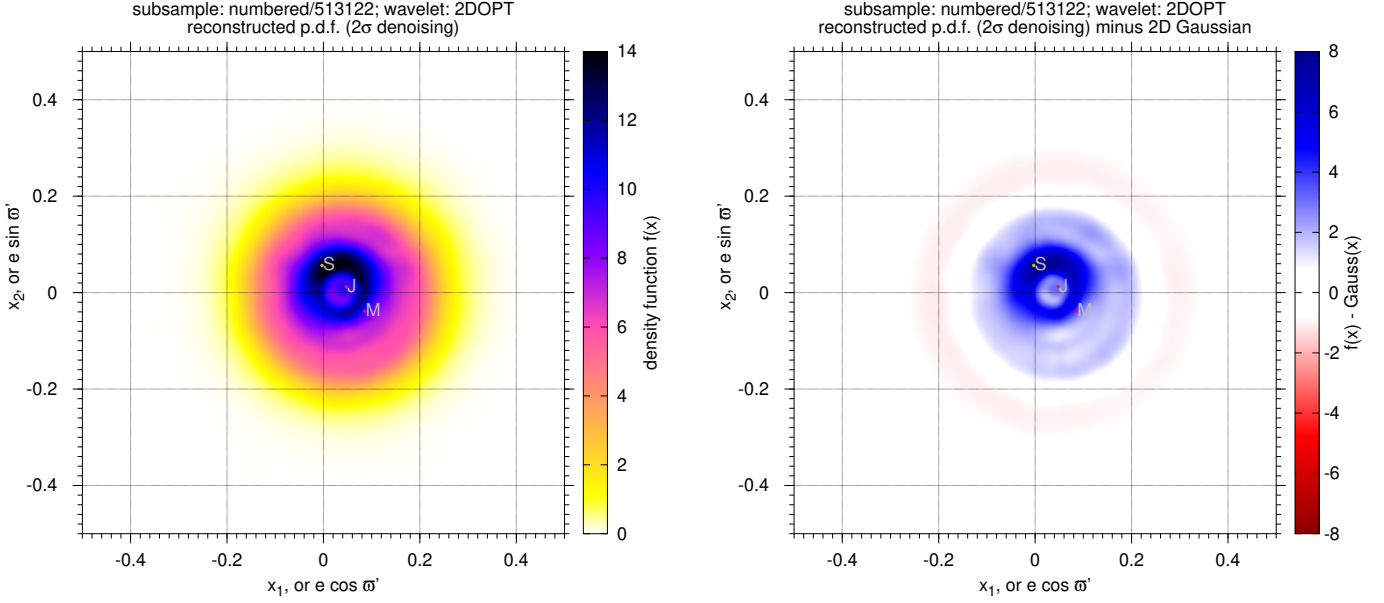


Figure 4: Reconstructed 2D p.d.f. model $\tilde{f}(x)$, and its deviation from the best fitting radially symmetric Gaussian, based on the CWT analysis from Fig. 3.

tent, but nevertheless, ways are possible to further increase the computing speed, which we consider as a work for future.

Another limitation is that our algorithm is entirely isotropic, i.e. it applies only radially symmetric wavelets with a radially symmetric (i.e. diagonal) scale matrix. This means that it does not suit well to analyse physically heterogeneous pairs of random quantities (because they may infer considerably different scales). The extension of the algorithm to non-isotropic cases is possible, however this results in an additional jump of dimensionality from 3 to 5. This would obviously increase the computational complexity further, possibly rendering the algorithm impractical.

Further ways to generalize this method may possibly involve a neat reduction of various statistical distortions, e.g. selection biases and more. This includes, in particular, the so-called unknown inclination effect in the mass distribution of exoplanets (those detected by radial velocity technique), and in the stellar rotation velocities. In the both cases, we actually measure a distorted quantity, $m' = m \sin i$ or $v' = v \sin i$ in place of m or v , where i is some inclination angle. The latter inclination is unknown in individual cases, but its effect on the observed distributions $f(m)$ or $f(v)$ can be reduced in a statistical

sense. It appears that if the inclination i is isotropically distributed then the p.d.f. for m and for m' become tied by an integral Abel equation. Solving this integral equation is an ill-posed task, but we believe that our wavelet analysis technique might be useful to invert that integral in a regularized manner.

Also, our method may be improved to take into account measurement uncertainties in the input sample (which are currently assumed mathematically accurate).

Acknowledgements

This work was supported by the Russian Foundation for Basic Research grant 17-02-00542 A and by the Presidium of Russian Academy of Sciences programme P-28, subprogramme “The space: investigating fundamental processes and their interrelations”.

Appendix A. Deriving the general isotropic CWT inversion formula

Let us seek the inverse wavelet transform for (10) in the form:

$$g(x) = \int_0^{+\infty} p(\kappa) d\kappa \int_{\mathbb{R}^n} \Upsilon(\kappa, c) \gamma(\kappa x + c) dc, \quad (\text{A.1})$$

where $p(\kappa)$ and γ are unspecified functions. This formula by definition assumes radially symmetric wavelets ψ . The reconstruction kernel γ is also radially symmetric.

Applying the Fourier transform to (10) and (A.1), we obtain

$$\hat{Y}(\kappa, \omega) = \hat{f}^*(\kappa\omega)\hat{\psi}(\omega), \quad \hat{g}(\omega) = \hat{f}(\omega)\hat{h}(\omega), \quad (\text{A.2})$$

where

$$\hat{h}(\omega) = \int_0^{+\infty} \mu\left(\frac{\omega}{\kappa}\right) \frac{p(\kappa)d\kappa}{\kappa^n}, \quad \mu(s) = \hat{\gamma}(s)\hat{\psi}^*(s). \quad (\text{A.3})$$

Our goal is to achieve $\hat{h}(\omega) \equiv \text{const}$, then we would obtain $\hat{g} \equiv C\hat{f}$.

Remarkably, \hat{h} appeared radially symmetric as well. Now, perform a replacement $\kappa \mapsto \omega\kappa$:

$$\hat{h}(\omega) = \int_0^{+\infty} \mu(\kappa^{-1}) \frac{p(\omega\kappa)}{\omega^{n-1}\kappa^n} d\kappa. \quad (\text{A.4})$$

We may notice that

$$\text{if } p(s\kappa) \equiv s^{n-1}p(\kappa) \implies \hat{h}(\omega) = \text{const}, \quad (\text{A.5})$$

as we aimed to achieve. Therefore, $p(\kappa)$ must be homogeneous of degree $n - 1$. Since it is a function of a single-dimensional argument, it must be simply a power function $p(\kappa) = \kappa^{n-1}$. This implies $\hat{h}(\omega) \equiv C_{\psi\gamma}$. Now we only need to return back to the function originals to write down (11).

Notice that $\omega = 0$ is a peculiar point. From (A.3), we have $\hat{h}(0) = 0$ due to the required mutual admissibility property of γ and ψ . But all other values of \hat{h} are equal to $C_{\psi\gamma}$, by the construction of h . This appears because the Fubini theorem does not actually work when applying the Fourier transform to (A.1), so we cannot interchange the integrals legally, and (A.3) becomes invalid. The reason is because of the integrand behaviour near $\kappa = 0$:

$$p(\kappa)Y(\kappa, \mathbf{c})\gamma(\kappa\mathbf{x} + \mathbf{c}) \stackrel{\kappa \rightarrow 0}{\sim} \kappa^{n-1}\psi(\mathbf{c})\gamma(\kappa\mathbf{x} + \mathbf{c}). \quad (\text{A.6})$$

By integrating its absolute value by \mathbf{x} , then by \mathbf{c} , we obtain

$$\kappa^{-1} \int |\psi(\mathbf{t})|d\mathbf{t} \int |\gamma(\mathbf{t})|d\mathbf{t}, \quad (\text{A.7})$$

which cannot be integrated further with respect to κ , because $\int d\kappa/\kappa$ does not converge near $\kappa = 0$. Hence, the absolute convergence is broken and the Fubini theorem cannot be applied directly, while all the derivation above appears merely symbolic.

To make this derivation more mathematically rigorous, we need to replace the low limit in the outer integral of (A.1) by some $\kappa_{\min} > 0$ and then consider the limit for $\kappa_{\min} \rightarrow 0$. In this case (A.3) becomes legal, with the lower limit replaced by κ_{\min} , and in (A.4) the lower limit should be κ_{\min}/ω . Finally,

$$\hat{h}(\omega) = \int_0^{a_{\max}\omega} \mu(s) \frac{ds}{s}, \quad (\text{A.8})$$

where $a_{\max} = 1/\kappa_{\min}$. As we can see, this $\hat{h}(\omega)$ is no longer strictly constant, although for large a_{\max} it is almost constant for $\omega \gg 1/a_{\max}$. As a_{\max} tends to infinity, the limit of $\hat{h}(\omega)$ is $C_{\psi\gamma}$ for all $\omega \neq 0$, but the point $\omega = 0$ always remains special.

Whether or not this peculiarity is important, depends on the properties of $f(\mathbf{x})$. The inverse wavelet transform may be unable to correctly reconstruct some ‘infinite-scale’ structure of f : constant offset, trends, etc. This is not very surprising, because e.g. if $\int \psi = 0$ than any constant offset, added to $f(\mathbf{x})$, is basically ‘killed’ by the CWT, so it cannot be reconstructed by the inversion formula. In fact, any harmonic function f_0 , i.e. any solution of the Laplace equation $\Delta f_0(\mathbf{x}) = 0$, would be ‘killed’ by the CWT, if we choose $\psi = \Delta\varphi$. In this case, the formula (A.1) may produce some $g(\mathbf{x}) = f(\mathbf{x}) - f_0(\mathbf{x})$ with an unknown harmonic f_0 . What this g could be? By the Liouville theorem, a harmonic function f_0 cannot be bounded (except if it is a constant), but g must be bounded thanks to the wavelet localization property. So in general the inversion formula (A.1) should result in a bounded non-harmonic remnant of $f(\mathbf{x})$. But if $f(\mathbf{x})$ is a distribution density then it is necessarily bounded and well-localized. Then the formula (A.1) would reconstruct it literally, without any distortions, because such a function cannot contain any ‘infinite-scale’ structure mentioned above.

We do not give a formal mathematical proof for this conclusion, since mathematical theory is beyond the scope of this paper, but this subtle matter needs a

detailed discussion from the practical point of view.

For example, if $\hat{h}(0) = 0$ then for any finite a_{\max} the reconstruction $f_{a_{\max}}(x)$ always integrates to zero. Hence, if the formula (11) is understood as a limit for $a_{\max} \rightarrow \infty$, would not this limit integrate to zero too? But $f(x)$ is a probability density, so it must integrate to unit. So what does this apparent contradiction mean in practice?

In practical tests it appeared that the reconstruction $f_{a_{\max}}(x)$ has very long (about a_{\max}) but small negative tails, while closely following $f(x)$ in the central part. Whenever $a_{\max} \rightarrow \infty$, the negative tails of the reconstruction become longer, simultaneously approaching zero. In the end, we obtain just $f(x)$ itself. Therefore, although all our partial reconstructions integrate to zero, their limit for $a_{\max} \rightarrow \infty$ equals to $f(x)$ and integrates to what $f(x)$ integrates, i.e. to unity. Mathematically, this apparent paradox just means that such convergence is not uniform, so we formally cannot interchange the integration with taking the limit:

$$\lim_{a_{\max} \rightarrow +\infty} \int_{\mathbb{R}^n} f_{a_{\max}}(\mathbf{x}) d\mathbf{x} \neq \int_{\mathbb{R}^n} \lim_{a_{\max} \rightarrow +\infty} f_{a_{\max}}(\mathbf{x}) d\mathbf{x}. \quad (\text{A.9})$$

So, whenever $f(x)$ is bounded and localized well enough (hence, does not have an ‘infinite-scale’ structure like non-zero constant level or a trend or other harmonic remnant), the inversion formula (11) should work literally, i.e. it should reconstruct f without any corruptions.

In practice, however, we cannot compute the limit, and always deal with some finite a_{\max} following from the discretization step of the κ variable.⁴ Therefore, all p.d.f. reconstructions that we are able to compute from (11) numerically, would integrate to zero and would then have small but long negative tails. Formally, such a behaviour is non-physical, because the probability cannot be negative. However, in practice these negative tails remain small in absolute magnitude, so they just can be neglected. In fact, this is done automatically if $f(x)$ is computed in the range much smaller than a_{\max} . Moreover, the remaining ‘kernel’ part of the reconstruction automatically appears to integrate close to unit.

⁴Our code implies $a_{\max} \sim 3\sigma/h$.

Appendix B. 2D wavelet transform of radially symmetric Gaussian and flat distributions

Using the definition (10), let us substitute a radially symmetric p.d.f.:

$$Y(a, \mathbf{b}) = \int_{\mathbb{R}^n} f(x) \psi\left(\frac{|\mathbf{x} - \mathbf{b}|}{a}\right) d\mathbf{x}. \quad (\text{B.1})$$

Applying a replacement $\mathbf{t} = (\mathbf{x} - \mathbf{b})/a$ and using spherical parametrization, this can be rewritten in two equivalent forms,

$$Y(a, b) = a^n \int_0^{+\infty} \psi(t) t^{n-1} dt \oint f\left(\sqrt{a^2 t^2 + b^2 + 2abt \cos \theta}\right) d\Omega, \quad (\text{B.2})$$

where θ is the angle between \mathbf{t} and \mathbf{b} , while Ω is the solid angle in \mathbb{R}^n , which is integrated over the entire unit sphere \mathcal{S}_n . Notice that Y now depends only on the scalar arguments a and b , meaning it became radially symmetric with respect to \mathbf{b} .

If $f(x)$ is a radially-symmetric flat distribution then we obtain

$$f(x) = \begin{cases} \frac{1}{S_n}, & x \leq 1, \\ 0, & x > 1, \end{cases} \implies Y(a, b) = a^n \int_0^{+\infty} \psi(t) t^{n-1} dt \int_{a^2 t^2 + b^2 + 2abt \cos \theta \leq 1} \frac{d\Omega}{S_n}, \quad (\text{B.3})$$

The condition in the inner integral is equivalent to a condition on the angle θ in the form

$$\cos \theta \leq \frac{1 - b^2 - a^2 t^2}{2abt}, \quad (\text{B.4})$$

which restrict some general solid angle, or a domain on the unit sphere. This domain depends on a , b , and t , and for some their values this domain may turn either empty or cover the complete sphere, because the right hand side of (B.4) may become smaller than -1 or above $+1$, respectively. So implicitly this inequality may also restrict the integration domain for t .

Notice that all of a , b , and t are non-negative numbers here. Using this property, after some el-

emetary manipulations we can set the following constraint on θ explicitly:

$$\begin{aligned} \theta \in [\pi - \theta_0, \pi + \theta_0], & \quad t \in \left[\frac{|b-1|}{a}, \frac{b+1}{a} \right], \\ \theta_0 = \arccos \frac{b^2 + a^2 t^2 - 1}{2abt}, & \\ \theta \in [0, 2\pi], & \quad t \in \left[0, \frac{1-b}{a} \right], \quad b < 1, \end{aligned} \quad (\text{B.5})$$

and empty set otherwise.

Therefore,

$$a^{-n} Y(a, b) = \int_0^{\frac{1-b}{a}} \psi(t) t^{n-1} dt + \int_{\frac{|b-1|}{a}}^{\frac{b+1}{a}} \psi(t) t^{n-1} dt \int_{|\pi-\theta| \leq \theta_0} \frac{d\Omega}{S_n}, \quad (\text{B.6})$$

where the first integral should be removed, if $b > 1$. In the 2D case, the integration with respect to $d\Omega$ is equivalent to integration over just θ , so the formula becomes

$$Y(a, b) = a^2 \int_0^{\frac{1-b}{a}} \psi(t) t dt + \frac{a^2}{\pi} \int_{\frac{|b-1|}{a}}^{\frac{b+1}{a}} \theta_0(t) \psi(t) t dt, \quad (\text{B.7})$$

Now, since $\psi(t) = \Delta\varphi(t)$, by the radial symmetry we have $\psi(t) = t^{-n} (t^n \varphi'(t))'$, and hence $\psi(t) t^{n-1} dt = d(t^n \varphi'(t))/t$. This allows us to derive the following identity:

$$\begin{aligned} Q_n(t) &:= \int q(t) \psi(t) t^{n-1} dt = \int \frac{q(t)}{t} d(t^n \varphi'(t)) \\ &= q\varphi' t^{n-1} - \int \left(\frac{q(t)}{t} \right)' t^n d\varphi(t) \\ &= q\varphi' t^{n-1} - \int (q' t^{n-1} - q t^{n-2}) d\varphi \\ &= q\varphi' t^{n-1} - \int q'(t) \varphi' t^{n-1} dt + \int q t^{n-2} d\varphi \\ &= (t\varphi' + \varphi) q t^{n-2} - \int q' \varphi' t^{n-1} dt - \int (q t^{n-2})' \varphi(t) dt \\ &= (t\varphi' + \varphi) q t^{n-2} - \int \left[(t\varphi' + \varphi) q' + \frac{n-2}{t} q\varphi \right] t^{n-2} dt. \end{aligned} \quad (\text{B.8})$$

For $n = 2$ this remarkably simplifies to just

$$Q_2(t) = (t\varphi' + \varphi)q - \int (t\varphi' + \varphi)q' dt, \quad (\text{B.9})$$

so the integration can be also understood with respect to q as independent variable (expressing t via q).

By substituting $q = 1$ and $q = \theta_0(t)$, we obtain:

$$\begin{aligned} a^{-2} Y(a, b) &= (t\varphi' + \varphi) \Big|_{t=\max(\frac{1-b}{a}, 0)} - \varphi(0) \\ &+ \frac{1}{\pi} [(t\varphi' + \varphi)\theta_0] \Big|_{\frac{|b-1|}{a}}^{\frac{b+1}{a}} - \frac{1}{\pi} \int_{\frac{|b-1|}{a}}^{\frac{b+1}{a}} (t\varphi' + \varphi)\theta_0' dt. \end{aligned} \quad (\text{B.10})$$

Now we may use the property that $\theta_0 = 0$ at the right endpoint, and θ_0 at the left endpoint is either 0, if $b > 1$, or π , if $b < 1$. Moreover, we can now apply a replacement of the integration variable $t \mapsto \theta_0$, so we have:

$$Y(a, b) = \begin{cases} -a^2 \varphi(0) + \frac{a^2}{\pi} \int_0^\pi (t\varphi' + \varphi) \Big|_{t=t_+(\theta)} d\theta, & b < 1, \\ \frac{a^2}{\pi} \int_0^{\arcsin \frac{1}{b}} (t\varphi' + \varphi) \Big|_{t=t_-(\theta)}^{t_+(\theta)} d\theta, & b > 1, \end{cases} \quad (\text{B.11})$$

$$t_\pm(\theta) = \frac{1}{a} \left(b \cos \theta \pm \sqrt{1 - b^2 \sin^2 \theta} \right).$$

These integrals can be computed numerically (we use the GNU scientific library for that).

Notice that if $b > 1$, one may mistakenly assume that in terms of θ the length of the integration segment becomes zero and hence the integral vanishes. This is wrong, because θ_0' changes sign at $t_* = \sqrt{b^2 - 1}/a$, if $b > 1$. We should split the integration segment into two portions, separated by this change point, and compute these integrals independently, assuming different solution branches for t , either $t_1(\theta)$ or $t_2(\theta)$.

Now let us consider the case of standard Gaussian density $f(x)$:

$$\begin{aligned} f(x) &= \frac{1}{(2\pi)^{\frac{n}{2}}} e^{-\frac{x^2}{2}} \implies \\ Y(a, b) &= a^n \int_0^{+\infty} \psi(t) t^{n-1} dt \oint e^{-\frac{a^2 t^2 + b^2}{2} - abt \cos \theta} \frac{d\Omega}{(2\pi)^{\frac{n}{2}}}, \end{aligned} \quad (\text{B.12})$$

which for $n = 2$ turns into

$$Y(a, b) = a^2 e^{-\frac{b^2}{2}} \int_0^{+\infty} e^{-\frac{a^2 t^2}{2}} \psi(t) dt \int_0^{2\pi} e^{-abt \cos \theta} \frac{d\theta}{2\pi}. \quad (\text{B.13})$$

The innermost integral can be expressed via the modified Bessel function I_0 , so we have

$$\begin{aligned} Y(a, b) &= a^2 e^{-\frac{b^2}{2}} \int_0^{+\infty} e^{-\frac{a^2 t^2}{2}} I_0(abt) \psi(t) dt \\ &= a^2 \int_0^{+\infty} e^{-\frac{(at-b)^2}{2}} \left[e^{-abt} I_0(abt) \right] \psi(t) dt \quad (\text{B.14}) \end{aligned}$$

The last formula was necessary to replace I_0 in the integrand by a normalized form $e^{-z} I_0(z)$, which is a bounded well-behaved function decreasing as $\sim 1/\sqrt{z}$ in the tail. This integral can be computed numerically.

In the both cases, we could not find a fully analytic representation of the wavelet transform, except for the 2DMHAT wavelet, for which the integral (B.14) was computed by means of computer algebra:

$$Y(a, b) = \left(\frac{a^2}{a^2 + 1} \right)^2 \left(2 - \frac{b^2}{a^2 + 1} \right) e^{-\frac{1}{2} \frac{b^2}{a^2 + 1}}. \quad (\text{B.15})$$

References

- Abramovich, F., Bailey, T.C., Sapatinas, T., 2000. Wavelet analysis and its statistical applications. *JRSS-D (The Statistician)* 49, 1–29.
- Azaïs, J.M., Delmas, C., 2002. Asymptotic expansions for the distribution of the maximum of Gaussian random fields. *Extremes* 5, 181–212.
- Baluev, R.V., 2013. Detecting non-sinusoidal periodicities in observational data: the von Mises periodogram for variable stars and exoplanetary transits. *MNRAS* 431, 1167–1179.
- Baluev, R.V., 2018. Statistical detection of patterns in unidimensional distributions by continuous wavelet transforms. *Astron. & Comp.* 23, 151–165.
- Baluev, R.V., Shaidulin, V.S., 2018. Fine-resolution wavelet analysis of exoplanetary distributions: hints of an overshooting iceline accumulation. *Ap&SS* 363, 192.
- Brown, A.G.A., Vallenari, A., Prusti, T., de Bruijne, J.H.J., Babusiaux, C., Bailer-Jones, C.A.L., et al., 2018. Gaia Data Release 2. Summary of the contents and survey properties. *A&A* 616, A1.
- Chereul, E., Cr ez e, M., Bienaym e, O., 1998. The distribution of nearby stars in phase space mapped by Hipparcos. II. Inhomogeneities among A-F type stars. *A&A* 340, 384–396.
- Fadda, D., Slezak, E., Bijaoui, A., 1998. Density estimation with nonparametric methods. *A&ASS* 127, 335–352.
- Foster, G., 1996. Wavelets for period analysis of unevenly spaced time series. *AJ* 112, 1709–1729.
- Grossman, A., Morlet, J., 1984. Decomposition of Hardy functions into square integrable wavelets of constant shape. *SIAM J. Math. Anal.* 15, 723–736.
- Hara, N.C., Bou e, G., Laskar, J., Correia, A.C.M., 2017. Radial velocity data analysis with compressed sensing techniques. *MNRAS* 464, 1220–1246.
- Kholshevnikov, K.V., Titov, V.B., 2007. Two-body problem [in Russian]. St. Pet. Univ. Press, St Petersburg.
- McEwen, J.D., Feeney, S.M., Peiris, H.V., Wiaux, Y., Ringeval, C., Bouchet, F.R., 2017. Wavelet-bayesian inference of cosmic strings embedded in the cosmic microwave background. *MNRAS* 472, 4081–4098.
- McEwen, J.D., Hobson, M.P., Lasenby, A.N., Mortlock, D.J., 2004. A high-significance detection of non-Gaussianity in the Wilkinson Microwave Anisotropy Probe 1-yr data using directional spherical wavelets. *MNRAS* 359, 1583–1596.
- Romeo, A.B., Horellou, C., Bergh, J., 2003. N-body simulations with two-orders-of-magnitude higher performance using wavelets. *MNRAS* 342, 337–344.
- Romeo, A.B., Horellou, C., Bergh, J., 2004. A wavelet add-on code for new-generation N-body simulations and data denoising (JOFILUREN). *MNRAS* 354, 1208–1222.
- Skuljan, J., Hearnshaw, J.B., Cottrell, P.L., 1999. Velocity distribution of stars in the solar neighbourhood. *MNRAS* 308, 731–740.
- Wang, N., Lu, C., 2010. Two-dimensional continuous wavelet analysis and its application to meteorological data. *J. Atmospheric & Oceanic Technology* 27, 652–666.